

¹
² Susceptible host dynamics explain pathogen resilience to
³ perturbations

⁴
⁵ Sang Woo Park, . . . , Sarah Cobey

⁶ Abstract

⁷ Major priority for epidemiological research in the time of anthropogenic change is
⁸ understanding how infectious disease dynamics respond to perturbations. Interven-
⁹ tions to slow the spread of SARS-CoV-2 significantly disrupted the transmission
¹⁰ of other human pathogens. As interventions lifted, whether and when respiratory
¹¹ pathogens would eventually return to their pre-pandemic dynamics remains to be
¹² answered. To address this gap, we develop a framework for estimating pathogen re-
¹³ silience based on how fast epidemic patterns return to their pre-pandemic, endemic
¹⁴ dynamics. Our analysis suggests that some pathogens may have settled to endemic
¹⁵ cycles that are different from their pre-pandemic patterns. Finally, we show that
¹⁶ the replenishment rate of the susceptible pool is a key determinant of pathogen re-
¹⁷ silience. Our framework offers a novel perspective to characterizing the dynamics of
¹⁸ endemic pathogens and their responses to SARS-CoV-2 interventions. [SWP: Need
¹⁹ to emphasize broader implications.]

Non-pharmaceutical interventions (NPIs) to slow the spread of SARS-CoV-2 disrupted the transmission of other human respiratory pathogens, adding uncertainties to their future epidemic dynamics and the overall public health burden [1]. As interventions lifted, large heterogeneities in outbreak dynamics were observed across different pathogens in different countries, with some pathogens exhibiting earlier resurgences than others [2, 3, 4]. Heterogeneities in the overall reduction in transmission and the timing of re-emergence likely reflect differences in NPI patterns, pathogen characteristics, immigration/importation from other countries, and pre-pandemic pathogen dynamics [5]. Therefore, comparing the differential impact of the pandemic NPIs across pathogens can provide unique opportunities to learn about underlying pathogen characteristics, such as their transmissibility or duration of immunity, from heterogeneities in re-emergence patterns [6].

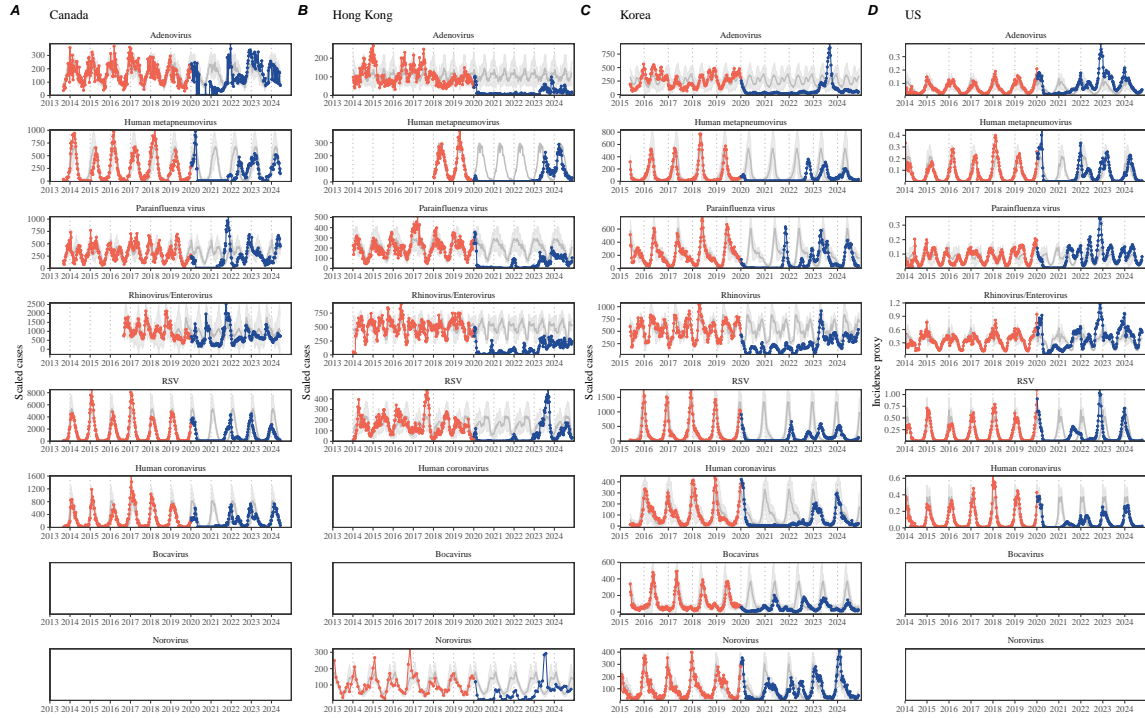


Figure 1: Observed heterogeneity in responses to COVID-19 pandemic across respiratory pathogens and norovirus in (A) Canada, (B) Hong Kong, (C) Korea, and (D) US. Red points and lines represent data before 2020. Blue points and lines represent data since 2020. Gray lines and shaded regions represent the mean seasonal patterns and corresponding 95% confidence intervals based on the observed outbreak patterns before 2020.

Even though more than five years have passed since the emergence of SARS-CoV-2, we still observe persistent changes in pathogen dynamics following the pandemic NPIs: for example, compared to pre-pandemic, seasonal patterns, human metapneumovirus and bocavirus in Korea are circulating at lower levels, whereas RSV in Korea

36 seem to exhibit different seasonality (Figure 1). These observations suggest a possi-
37 bility for a fundamental change in pathogen dynamics following the pandemic NPIs,
38 which can be driven by permanent shift in either human behavior or population-level
39 immunity [7, 8]. Moreover, the possibility of a long-lasting impact of the pandemic
40 NPIs pose an important question for future infectious disease dynamics: can we pre-
41 dict whether and when other respiratory pathogens will eventually return to their
42 pre-pandemic dynamics?

43 So far, the majority of epidemiological analyses of respiratory pathogens in the
44 context of the pandemic NPIs have focused on characterizing the timing of rebound
45 [1, 9, 5]. Instead, we seek to characterize how fast a pathogen returns to its pre-
46 pandemic dynamics. These two concepts have subtle but important differences: for
47 example, it took more than 3 years for human metapneumovirus to rebound in Hong
48 Kong but the observed epidemic patterns in 2024 are similar to pre-pandemic seasonal
49 means, suggesting a rapid return to pre-pandemic dynamics following a perturbation
50 (Figure 1). Measuring this rate of return is particularly useful because it allows us
51 to quantify the resilience of a host-pathogen system; in classical ecological literature,
52 resilience is defined as how fast a system returns to its stable, reference state following
53 a perturbation [10, 11, 12, 13].

54 To address this question, we propose a framework for characterizing the resilience
55 of a host-pathogen system based on how fast the system recovers from perturbation.
56 We begin by laying out a few representative scenarios that capture the potential im-
57 pact of COVID-19 interventions on endemic pathogen dynamics and illustrating how
58 resilience can be measured by comparing the pre- and post-pandemic dynamics of
59 susceptible and infected hosts. In practice, information on susceptible hosts are often
60 unavailable, and traditional methods for reconstructing the dynamics of susceptible
61 hosts require long-term endemic time series [14, 15], which cannot be applied due
62 to disruptions in epidemic patterns caused by COVID-19 interventions. Instead, we
63 utilize Takens' embedding theorem to reconstruct empirical attractors from data and
64 further measure the distance from this empirical attractor [16]. This reconstruction
65 allows us to characterize the rate at which this distance decreases over time, which
66 correspond to pathogen resilience. We apply this framework to analyzing pathogen
67 surveillance data for a wide array of respiratory and non-respiratory pathogens from
68 Canada, Hong Kong, Korea, and US. Finally, we show that susceptible host dynamics
69 are a key determinants of pathogen resilience. Our study offers unique insights into
70 understanding pathogen re-emergence patterns following COVID-19 interventions.

71 **Conceptual introduction to pathogen resilience**

72 In classical ecological literature, resilience of an ecological system is measured by
73 the rate at which the system returns to its reference state following a perturbation
74 [10, 11, 12, 13]. This rate corresponds to the largest real part of the eigenvalues of
75 the linearized system near equilibrium—here, we refer to this value as the *intrinsic*

resilience of the system, which represents the expected rate of return from perturbed states. However, respiratory pathogens often exhibit seasonal variation in transmission, meaning that the intrinsic resilience of a host-pathogen system varies across season. Nonetheless, we can still measure the *empirical* resilience of a host-pathogen system by looking at how fast the system returns to the pre-pandemic, endemic dynamics after interventions are lifted.

As an example, consider an intervention that reduce transmission by 50% for 6 months starting in 2020, which causes epidemic patterns to deviate from its original stable annual cycle for a short period of time and eventually come back (Figure 2A). To measure the empirical resilience of this system, we first need to be able to measure the distance from its pre-pandemic attractor. There are many different ways we can measure the distance from attractor, but for illustrative purposes, we choose one of the most parsimonious approach: that is, we look at how the susceptible (S) and infected (I) populations change over time and measure the distance on the SI phase plane (Figure 2B). In this simple case, the locally estimated scatterplot smoothing (LOESS) fit indicates that the distance from attractor decreases linearly on average (Figure 2C). Furthermore, the overall rate of return matches the intrinsic resilience of the seasonally unforced system (Figure 2C).

Alternatively, NPIs can permanently change our behavior and have persisting impact on the pathogen dynamics; as an example, we consider a scenario in which a 10% reduction in transmission persists even after the NPIs are lifted (Figure 2D–F). In such cases, we cannot know whether the pathogen will return to its original cycle or a different cycle until many years have passed after the NPIs are lifted, meaning that we cannot measure the distance against the new attractor that the system will eventually approach. Nonetheless, we can still measure the distance against the original, pre-pandemic attractor and ask how the distance changes over time (Figure 2E). The LOESS fit suggests that the distance from the attractor will initially decrease exponentially on average (equivalently, linearly on a log scale) and eventually plateau (Figure 2F). Here, a permanent 10% reduction in transmission rate slows down the system, which causes the distance from the attractor to decrease at a slower rate (Figure 2F) than it would have otherwise in the absence of permanent transmission reduction (Figure 2C). This example shows that resilience is not necessarily an intrinsic property of a specific pathogen. Instead, pathogen resilience is a property of a specific attractor that a host-pathogen system approaches, which depends on both pathogen and host characteristics.

Finally, transient phenomena can also complicate the picture (Figure 2G–I). For example, a stage-structured model for RSV initially exhibits a stable annual cycle, but perturbations from NPIs cause the epidemic to exhibit biennial cycles (Figure 2G). Despite this biennial cycle, we see that the system eventually approaches the original pre-pandemic attractor (Figure 2H), suggesting that this biennial cycle is a transient phenomenon. The LOESS fit indicates that the distance from the attractor will initially decrease exponentially at a rate that is consistent with the intrinsic resilience of the seasonally unforced system, but the rate of decrease slows down

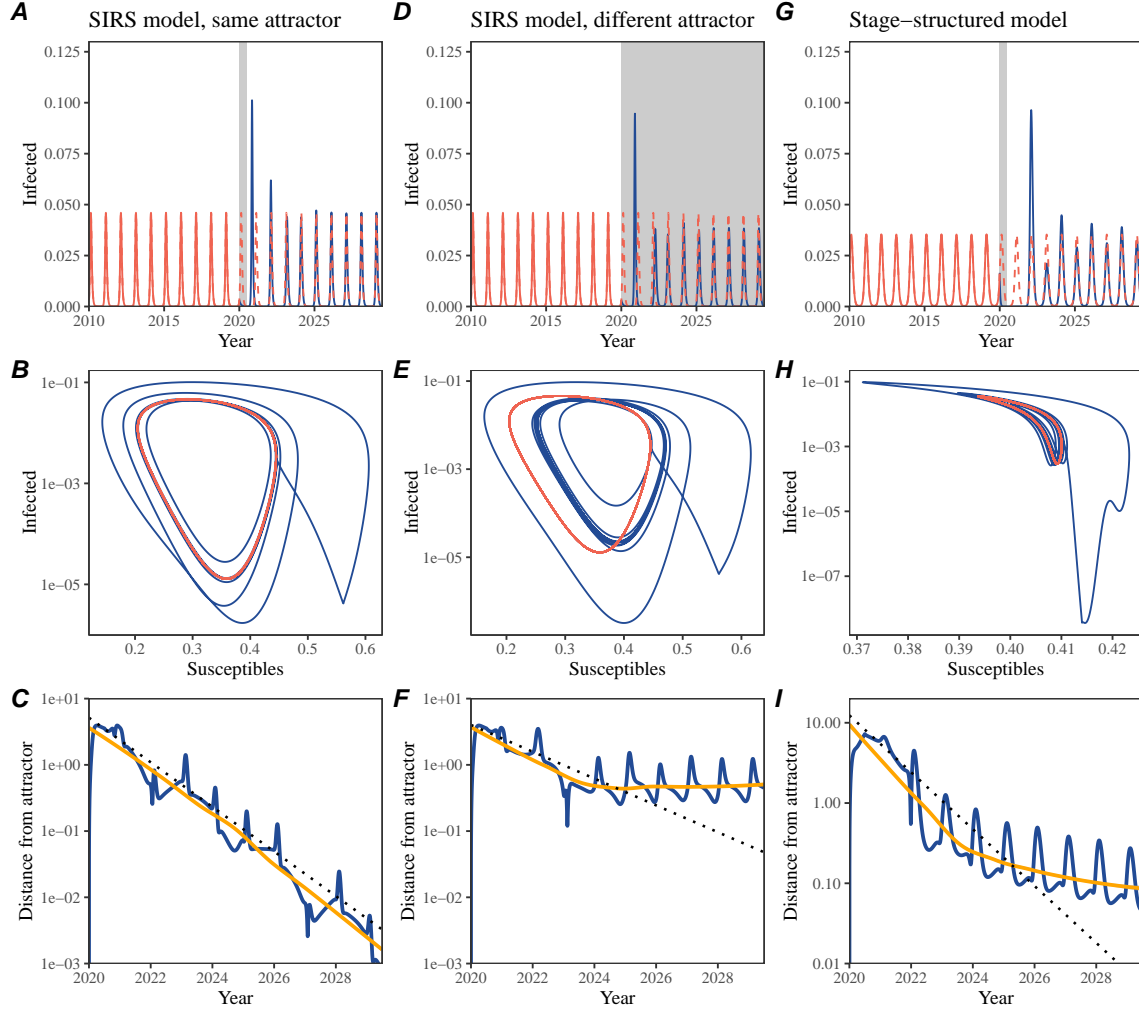


Figure 2: Conceptual framework for measuring pathogen resilience following NPIs across different scenarios. (A, D, G) Simulated epidemic trajectories across various models. Red and blue solid lines represent epidemic dynamics before and after interventions are introduced, respectively. Red dashed lines represent counterfactual epidemic dynamics in the absence of interventions. Gray regions indicate the duration of interventions. (B, E, H) Phase plane representation of the corresponding model. Red and blue solid lines represent epidemic trajectories on an SI phase plane before and after interventions are introduced, respectively. (C, F, I) Changes in logged distance from attractor over time. Blue lines represent the logged distance from attractor. Orange lines represent the locally estimated scatterplot smoothing (LOESS) fits to the logged distance from attractor. Dotted lines are superimposed as a comparison to have the same slope as the intrinsic resilience of the seasonally unforced system.

as the epidemic exhibits a biennial cycle (Figure 2I). In classical ecological theory,

120 this behavior is also referred to as a ghost attractor, which causes long transient
121 dynamics and slow transitions [17]. As we show in Supplementary Figure S1, strong
122 seasonal forcing in transmission can also lead to transient phenomena for a simple
123 SIRS model, causing a slowing down of the system.

124 In Supplementary Materials, we also explore measuring the resilience of a two-
125 strain host-pathogen system: when the dynamics two strains (or two pathogens) are
126 coupled through cross immunity, we would expect the entire system to be character-
127 ized by a single resilience value (rather than having two separate resilience for each
128 strain). Simulations from a simple two-strain system illustrate that separate anal-
129 yses of individual strain dynamics (e.g., RSV A vs B) and a joint analysis of total
130 infections (e.g., total RSV infections) yield identical resilience estimates, confirming
131 our expectation (Supplementary Figure S2, 3). Analogous to a single system, strong
132 seasonal forcing in transmission can cause the system to slow down through transient
133 phenomena (Supplementary Figure S4).

134 These observations indicate three possibilities. First, we can directly estimate
135 the empirical resilience of a host-pathogen system by looking at how fast the system
136 approaches a pre-pandemic attractor, provided that we can measure the distance
137 from attractor. The empirical approach to estimating pathogen resilience is partic-
138 ularly convenient because it does not require us to know the true underlying model.
139 As we show in Supplementary Figure S5, estimating the intrinsic resilience from fit-
140 ting standard compartmental models can lead to biased estimates, especially under
141 model misspecification. Second, resilience estimates allow us to make phenomenolog-
142 ical predictions about the dynamics of a host-pathogen system following a perturba-
143 tion: assuming that the distance from the attractor will decrease exponentially over
144 time, we can obtain a ballpark estimate for when the system will reach an attractor.
145 Finally, deviation from an exponential decrease in the distance from attractor can
146 provide information about whether the system has reached an alternative attractor,
147 or a ghost attractor, that is different from the original, pre-pandemic attractor. These
148 alternative attractors may reflect continued perturbations from permanent changes
149 in transmission patterns as well as changes in immune landscapes.

150 **Inferring pathogen resilience from real data**

151 Based on these observations, we now set out to infer pathogen resilience from real
152 data. Here, we briefly lay out our approach to estimating pathogen resilience from
153 real data (Figure 3). We then test this approach against simulations and apply it to
154 real data.

155 So far, we focused on simple examples that assume a constant transmission re-
156 duction. However, in practice, the impact of NPIs on pathogen transmission is
157 likely more complex (Figure 3A), reflecting introduction and relaxation of various
158 intervention strategies. These complexities can lead to longer delays between the
159 introduction of NPIs and pathogen re-emergence as well as temporal variation in

outbreak sizes (Figure 3B): in this example, continued transmission reduction from NPIs limits the size of the first outbreak in 2021 following the emergence, allowing for a larger outbreak in 2022 when NPIs are further relaxed.

Previously, we relied on the dynamics of susceptible and infected hosts to compute the distance from attractor (Figure 2), but information on susceptible hosts are often not available in practice. In addition, uncertainties in case counts due to observation error as well as the possibility of complex, multiannual attractor adds challenges to measuring the distance from attractor. To address these challenges, we first reconstruct an empirical attractor by utilizing Takens' theorem, which states that an attractor of a nonlinear multidimensional system can be mapped onto a delayed embedding [16]. Here, we use delayed copies of logged values of pre-pandemic cases $C(t)$ (Figure 3C) to reconstruct the attractor:

$$\langle \log(C(t) + 1), \log(C(t - \tau) + 1), \dots, \log(C(t - (M - 1)\tau) + 1) \rangle, \quad (1)$$

where the delay τ and embedding dimension M are determined based on autocorrelations and false nearest neighbors, respectively [18, 19]. We then apply the same delay and embedding dimensions to the entire time series to determine the position on a multi-dimensional state space (Figure 3D), which allows us to measure the nearest neighbor distance between the current state of the system and the empirical attractor (Figure 3E). In principle, we can quantify how fast this distance decreases by fitting a linear regression on a log scale, where the slope of the linear regression corresponds to pathogen resilience. As we show in Supplementary Figure S6, overall temporal variations in the distance from attractor, especially the observed rate of decrease, appear robust to choices about embedding delays and dimensions; we note that using longer delays and higher dimensions tend to smooth out temporal variations in the distance from attractor.

Complex changes in the distance from attractor suggest that estimating pathogen resilience from linear regression will likely be sensitive to our choice of fitting windows for the regression. In Supplementary Materials, we explore an automated window selection criteria for linear regression and test it against randomized, stochastic simulations across a wide range of realistic NPI shapes. We find that resilience estimates based on the automated window selection criteria are moderately correlated (0.48) with the intrinsic resilience of the post-NPI attractor (Supplementary Figure S7). In contrast, a naive approach that uses the entire time series, starting from the peak distance, only gives a correlation of 0.09 and consistently underestimates the intrinsic resilience (Supplementary Figure S7).

Now, we apply this approach to pathogen surveillance data presented in Figure 1. For each time series, we apply Takens' theorem independently to reconstruct the empirical attractor and obtain the corresponding time series of distance from attractors (Supplementary Figure S8 for the distance time series and linear regression fits). Then, we use the automated window selection criteria to fit a linear regression and estimate the empirical resilience for each pathogen in each country. For most respiratory pathogens, resilience estimates fall between 0.4/year and 1.8/year (Figure

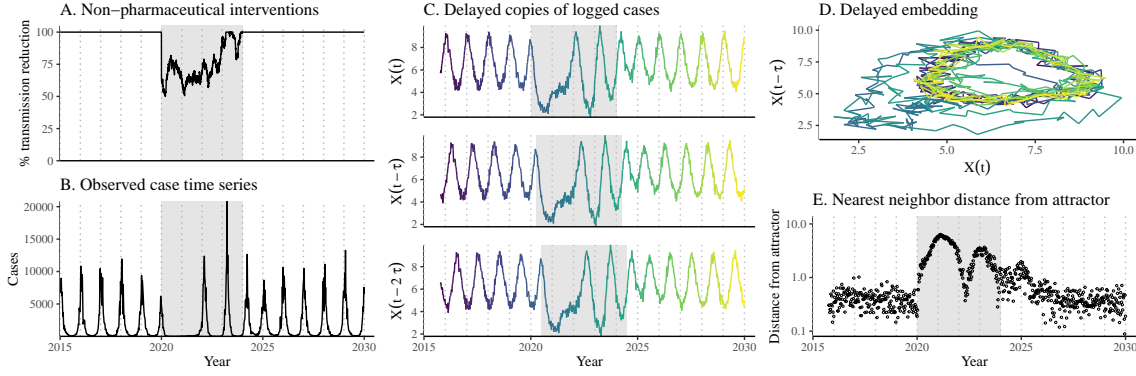


Figure 3: **A schematic diagram explaining how pathogen resilience can be inferred from real data.** (A) A realistic example of a synthetic NPI, represented by a relative reduction in transmission. (B) The impact of the synthetic NPI on epidemic dynamics simulated using a stochastic SIRS model. (C) Generating delayed copies of the logged time series allows us to obtain an embedding. (D) Two dimensional representation of an embedding. (E) Delayed embedding allows us to calculate the nearest neighbor distance from the empirical attractor, which is determined based on the pre-pandemic time series. This distance time series can be used to infer pathogen resilience by fitting a linear regression after choosing an appropriate window for regression.

201 4A), with the exception of Rhinovirus in the US (0.066/year; 95% CI: 0.018/year–
 202 0.113/year) and Bocavirus in Korea (0.087/year; 95% CI: 0.023/year–0.151/year).
 203 Excluding these exceptions, the mean resilience of common respiratory pathogens is
 204 0.974/year (95% CI: 0.784/year–1.16/year). As a reference, this is ≈ 7 times higher
 205 than the intrinsic resilience of pre-vaccination measles dynamics ($\approx 0.13/\text{year}$). Fi-
 206 nally, resilience estimates for norovirus appears to be comparable to the intrinsic
 207 resilience of measles: 0.119/year (95%CI: 0.004/year–0.233/year) for Korea and
 208 0.385/year (95% CI: 0.167/year–0.603/year). A simple ANOVA shows that there
 209 are significant differences in resilience estimates across countries ($p < 0.036$) and
 210 pathogens ($p < 0.030$).

211 Using resilience estimates, we now predict when each pathogen will return to
 212 their original pre-pandemic cycles. Specifically, we extend our linear regression fits
 213 to distance-from-attractor time series and ask when the predicted regression line
 214 will cross a threshold value, which we set to a mean of pre-pandemic distances. We
 215 predict that a return to pre-pandemic cycles would be imminent for most pathogens
 216 (Figure 4B; see Supplementary Figure S9 for a zoomed out version). In addition, we
 217 also predict that many pathogens should have already returned to their pre-pandemic
 218 dynamics by the end of 2024; but these predictions contradict some of the observed
 219 pathogen dynamics. For example, we predict that both human metapneumovirus and
 220 RSV in Korea should have returned to their attractors by now, but the magnitude
 221 and timing of recent epidemics are different from pre-pandemic patterns (Figure 1).

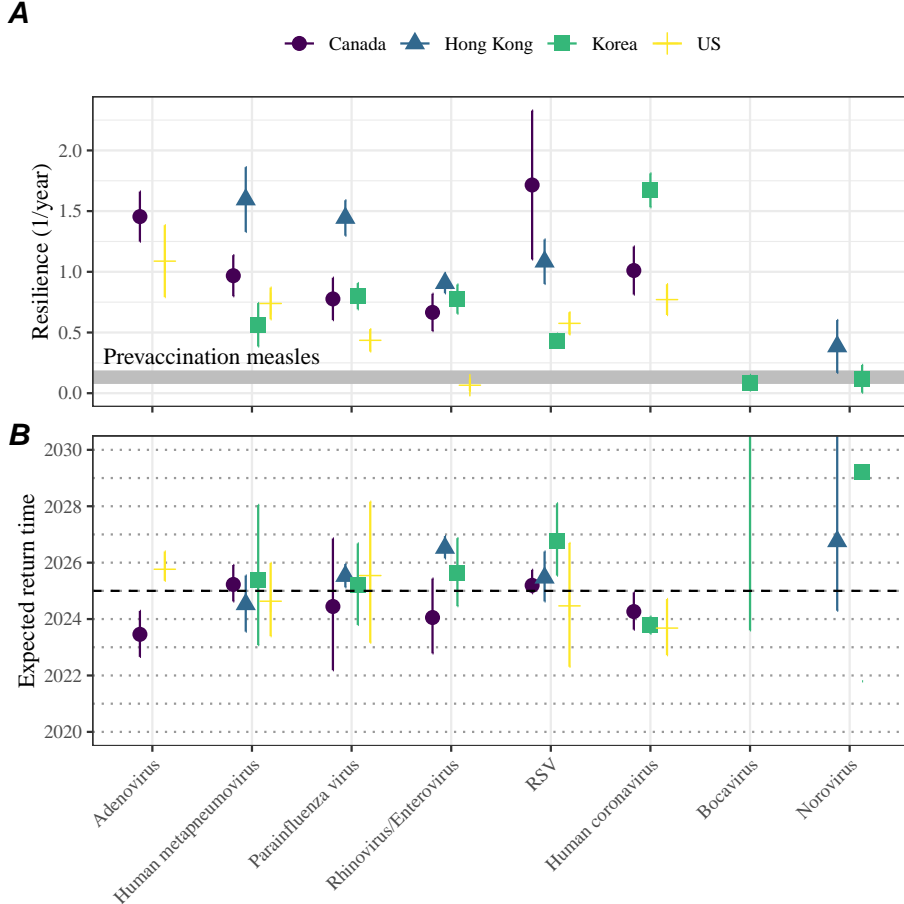


Figure 4: **Summary of resilience estimates.** (A) Estimated pathogen resilience. The gray horizontal line represents the intrinsic resilience of pre-vaccination measles dynamics. (B) Predicted timing of when each pathogen will return to their pre-pandemic cycles. The dashed line in panel B indicates the end of 2024 (current observation time). Error bars represent 95% confidence intervals.

222 These observations suggest the possibility that some common respiratory pathogens
 223 may have converged to different attractors.

224 In Supplementary Materials, we also consider using a lower threshold for the false
 225 nearest neighbor approach when determining the embedding dimension; this gives
 226 a higher embedding dimension. As explained earlier (Supplementary Figure S6),
 227 this gives a smoother distance-from-attractor time series (compare Supplementary
 228 Figure S10 with S8); this also requires us to use longer time series, which prevents
 229 us from estimating resilience for some pathogens. Overall, resulting estimates of
 230 pathogen resilience with higher embedding dimensions still fall between 0.3/year
 231 and 2.1/year for the most part (Supplementary Figure S11). A direct comparison
 232 between two approaches (i.e., original estimate vs using higher dimensions) shows a

233 strong consistency in resilience estimates (Supplementary Figure S12).

234 Susceptible host dynamics explain variation in pathogen 235 resilience

236 So far, we focused on quantifying pathogen resilience from the observed patterns of
237 pathogen re-emergence following COVID-19 interventions. But what factors deter-
238 mine how resilient a host-pathogen system is? Here, we use a standard Susceptible-
239 Infected-Recovered-Susceptible (SIRS) model to show that susceptible host dynamics
240 are the key determinants of pathogen resilience. To do so, we vary the basic reproduc-
241 tion number \mathcal{R}_0 , which represents the average number of secondary infections caused
242 by a newly infected individual in a fully susceptible population, and the duration of
243 immunity and compute intrinsic resilience for each parameter.

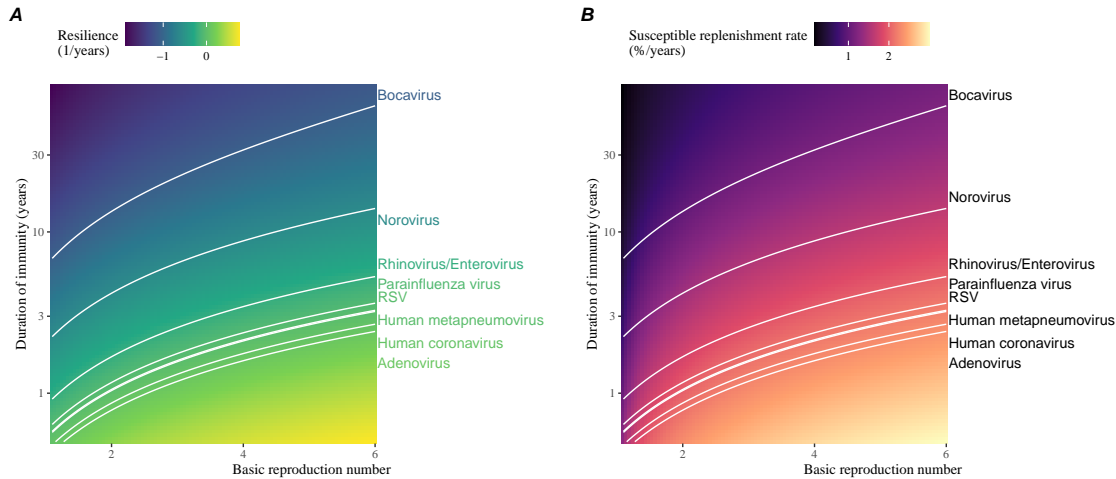


Figure 5: **Linking pathogen resilience to epidemiological parameters and susceptible host dynamics.** (A) The heat map represents intrinsic resilience as a function of the basic reproduction number \mathcal{R}_0 and the duration of immunity. (B) The heat map represents per-capita susceptible replenishment rate as a function of the basic reproduction number \mathcal{R}_0 and the duration of immunity. The standard SIRS model is used to compute intrinsic resilience and per-capita susceptible replenishment rate. Lines correspond to a set of parameters that are consistent with mean resilience estimates for each pathogen. Pathogens are ranked based on their mean resilience estimates, averaged across different countries.

244 We find an increase in \mathcal{R}_0 and a decrease in duration of immunity correspond
245 to an increase in pathogen resilience (Figure 5A). These variations can be under-
246 stood in terms of the susceptible host dynamics, where faster per-capita susceptible
247 replenishment rate causes the system to be more resilient (Figure 5B). This rate can

248 be expressed as a ratio between absolute rate at which new susceptibles enter the
249 population and the equilibrium number of susceptible individuals in the population,
250 \bar{S} . Therefore, both higher \mathcal{R}_0 and shorter duration of immunity can drive faster
251 per-capita susceptible replenishment rate (Figure 5B), especially because higher \mathcal{R}_0
252 leads to lower \bar{S} .

253 Finally, we can now rank different pathogens based on the average values of em-
254 pirical resilience, which allows us to determine a set of parameters that are consistent
255 with the estimated resilience (Figure 5A). Across all pathogens we consider, except
256 for bocavirus and norovirus, we estimate that the average duration of immunity is
257 likely to be short (< 6 years) across a plausible range of \mathcal{R}_0 . These rankings further
258 allow us to map each pathogen onto a set of parameters that are consistent with
259 its empirical resilience (Figure 5A) and obtain a plausible range of susceptible re-
260 plenishment rates for each pathogen (Figure 5B). However, we note that there is no
261 one-to-one correspondence between susceptible replenishment rates and pathogen re-
262 silience, leading to a wide uncertainty in the estimates for susceptible replenishment
263 rates (Figure 5B).

264 Discussion

265 The COVID-19 interventions have caused major disruptions to circulation patterns
266 of both respiratory and non-respiratory pathogens, adding challenges to predicting
267 their future dynamics [1, 2, 3, 4]. On the other hand, these interventions offer
268 large-scale natural experiments for understanding how different pathogens respond to
269 perturbations. In this study, we show that pathogen re-emergence patterns following
270 COVID-19 interventions can be characterized through the lens of ecological resilience.
271 Traditionally, ecological resilience measures how fast a system returns to a reference
272 state following a perturbation. In the context of respiratory pathogens, resilience
273 measures how fast epidemics return to their endemic cycles after interventions are
274 lifted.

275 We use an attractor reconstruction approach to quantify how distance from at-
276 tractor changes over time for each pathogen [16]. We show that the resilience of
277 a host-pathogen system can be estimated by fitting a linear regression to a logged
278 distance-from-attractor time series. Overall, we estimate that the resilience for most
279 common respiratory pathogens ranges between 0.4/year and 1.8/year, which is 3–14
280 times more resilient than prevaccination measles, indicating potential challenges in
281 controlling common respiratory pathogens.

282 Our framework allows us to make phenomenological predictions about when each
283 pathogen will return to their endemic cycles. The ability to predict future epidemic
284 patterns from resilience estimates offers a new paradigm for epidemic forecasting.
285 While this approach cannot predict the exact timing of outbreaks or epidemic pat-
286 terns, it is nonetheless useful for predicting when epidemics will settle down to regular
287 cycles after a large perturbation, such as COVID-19 interventions.

Our analyses suggest a possibility that several pathogens may have converged to different endemic cycles compared to their pre-pandemic epidemic patterns. Key examples include human metapnuemovirus, RSV, and bocavirus in Korea as well as RSV in Hong Kong. These changes may reflect changes in surveillance or actual shift in the dynamics, caused by permanent changes in behavior or population-level immunity. While it seems unlikely that permanent changes in behavior would only affect a few pathogens and not others, we cannot rule out this possibility given heterogeneity in the age of infection across different respiratory pathogens [SWP: CITE]. A shift in population-level immunity is plausible, as the emergence of SARS-CoV-2 and extinction of influenza B/Yamagata likely caused major changes in immune landscapes; interactions among co-circulating pathogens, such as cross immunity between RSV and HMPV [20], may have also contributed to changes in population-level immunity. However, we currently do not know how immunity, or lack thereof, from these pathogens would affect infection from other pathogens. Future studies should use detailed mechanistic models, coupled with behavioral and immunological data, to test these hypotheses and better understand post-pandemic dynamics of endemic pathogens.

We show that susceptible host dynamics shape pathogen resilience, where faster replenishment of the susceptible population causes the pathogen to be more resilient. For simplicity, we focus on waning immunity and birth as a main driver of the susceptible host dynamics but other mechanisms can also contribute to the replenishment of the susceptible population. In particular, pathogen evolution, especially the emergence of antigenically novel strains, can cause effective waning of immunity in the population; therefore, we hypothesize that faster rates of antigenic evolution can also cause a pathogen to be more resilient. Future studies should explore the relationship between the rate of evolution and resilience for antigenically evolving pathogens.

Quantifying pathogen resilience also offers novel approaches to validating population-level epidemiological models. So far, the majority of model validation in epidemiology is based on the ability of a model to reproduce the observed epidemic dynamics and to predict future dynamics [21, 20, 22, 23, 24]. However, there can be plethora of models that meet these criteria. For example, two major RSV models have been proposed so far to explain biennial epidemic patterns: (1) a stage- and age-structured model that allows for disease severity to vary with number of past infections and age of infection [22] and (2) a pathogen-interaction model that accounts for cross immunity between RSV and human metapnuemovirus [20]. Since both models can accurately reproduce the observed epidemic patterns, standard criteria for model validation do not allow us to distinguish between these two models from population-level data alone. Instead, we can measure the empirical resilience of each model by simulating various perturbations and compare them to estimates of empirical resilience from data, using COVID-19 interventions as an opportunity. Future studies should further investigate using pathogen resilience for validating epidemic models.

There are several limitations to our work. First of all, we did not extensively explore other approaches to reconstructing the attractor. Recent studies showed that

more sophisticated approaches, such as using non-uniform embedding, can provide more robust reconstruction for noisy data [19]. In the context of causal inference, choices about embedding can have major impact on the resulting inference [25]. Our resilience estimates are likely overly confident given a lack of uncertainties in attractor reconstruction as well as the simplicity of our statistical framework. Short pre-pandemic time series also contributes to the crudeness of our estimates. Nonetheless, as illustrated in our sensitivity analyses (Supplementary Figure S6, S10–S12), inferences about pathogen resilience appear to be robust to decisions about embedding lags and dimensions—this is because tracking the rate at which the system approaches the attractor is likely a much simpler problem than making inferences about causal directionality. Our qualitative prediction that common respiratory pathogens are more resilient than prevaccination measles is also likely to be robust to these predictions, given how rapid many respiratory pathogens returned to their original cycles following COVID-19 interventions.

Predicting the impact of anthropogenic changes on infectious disease dynamics is a fundamental aim of infectious disease research in a rapidly changing world. Our study illustrates that quantifying pathogen resilience can help us understand how infectious disease pathogens respond to major perturbations caused by public health interventions. More broadly, a detailed understanding of the determinants of pathogen resilience may offer unique insights into pathogen persistence and controllability.

Materials and Methods

Data

We gathered time series on respiratory infections from four different countries: Canada, Hong Kong, Korea, and United States (US). As a reference, we also included time series data on norovirus infections for available countries—in contrast to respiratory pathogens, we expect gastrointestinal viruses, such as norovirus, to be less affected by COVID-19 intervention measures. For all time series, we rounded every year to 52 weeks by taking the average number of cases and tests between the 52nd and 53rd week. We also rescale all time series to account for changes in testing patterns, which are then used for the actual analysis.

Weekly time series of respiratory infection cases in Canada comes from the Respiratory Virus Detection Surveillance System, which collect data from select laboratories across Canada. We extract the data from <https://www.canada.ca/en/public-health/services/surveillance/respiratory-virus-detections-canada.html>. To account for an increase in testing from 2013 to 2024, we calculate a 2 year moving average for the number of tests for each pathogen, which we use as a proxy for testing effort. Then, we divide the smoothed testing patterns by the smoothed value at the final week such that the testing effort has a maximum of 1. We then divide weekly cases by the testing effort to obtain a scaled case time series. A similar

371 approach was used earlier for the analysis of RSV time series in the US [22].

372 Weekly time series of respiratory infection cases in Hong Kong comes from the
373 Centre for Health Protection, Department of Health. We extract the data from
374 <https://www.chp.gov.hk/en/statistics/data/10/641/642/2274.html>. We also
375 apply the same scaling procedure to the time series as we did for Canada. For Hong
376 Kong, we only adjust for testing efforts up to the end of 2019 because there was a
377 major reduction in testing for common respiratory pathogens since 2020.

378 Weekly time series of acute respiratory infection cases in Korea comes from Ko-
379 rea Disease Control and Prevention Agency. We extract the data from <https://dportal.kdca.go.kr/pot/is/st/ari.do>. While we do not have information on
380 testing, the reported number of respiratory infections consistently increased from
381 2013 to the end of 2019, which we interpreted as changes in testing patterns. Since
382 we do not have testing numbers, we used the weekly sum of all acute respiratory vi-
383 ral infection cases as a proxy for testing, which were further smoothed with moving
384 averaged and scaled to have a maximum of 1. For Korea, we also only adjust for
385 testing efforts up to the end of 2019.

386 Finally, weekly time series of respiratory infection cases in the US comes from
387 the National Respiratory and Enteric Virus Surveillance System. In the US, there
388 has been a large increase in testing against some respiratory pathogens, especially
389 RSV, which could not be corrected for through simple scaling. Instead, we derive an
390 incidence proxy by multiplying the test positivity with influenza-like illness positivity,
391 which is taken from <https://gis.cdc.gov/grasp/fluvview/fluportaldashboard.html>. This method of estimating an incidence proxy has been recently applied in
392 the analysis of seasonal coronaviruses [7] and Mycoplasma pneumoniae infections [4].
393 Detailed assumptions and justifications are provided in [26].

396 Estimating pathogen resilience

397 In order to measure pathogen resilience from surveillance data, we first reconstruct
398 the empirical pre-pandemic attractor of the system using Takens' embedding theorem
399 [16]. Specifically, for a given pathogen, we take the pre-pandemic (before 2020)
400 case time series $C(t)$ and reconstruct the attractor using delayed embedding with a
401 uniform delay of τ and dimension M :

$$X_{\tau,m}(t) = \langle \log(C(t) + 1), \log(C(t - \tau) + 1), \dots, \log(C(t - (M - 1)\tau) + 1) \rangle. \quad (2)$$

402 Here, the delay τ is determined by looking at the autocorrelation of the logged pre-
403 pandemic time series and asking when the autocorrelation crosses 0 for the first time
404 [19]; a typical delay for an annual outbreak is around 13 weeks.

405 Then, for a given delay τ , we determine the embedding dimension M using the
406 false nearest neighbors approach [18, 19]. To do so, we start with an embedding
407 dimension e and construct a set of points $A_{\tau,e} = \{X_{\tau,e}(t) | t < 2020\}$. Then, for
408 each point $X_{\tau,e}(t)$, we determine the nearest neighbor from the set $A_{\tau,e}$, which we
409 denote $X_{\tau,e}(t_{nn})$ for $t \neq t_{nn}$. Then, if the distance between these two points on $e + 1$

dimension, $D_{\tau,e+1}(t) = \|X_{\tau,e+1}(t_{nn}) - X_{\tau,e+1}(t)\|_2$, is larger than their distance on e dimension, $D_{\tau,e}(t) = \|X_{\tau,e}(t_{nn}) - X_{\tau,e}(t)\|_2$, these two points are deemed to be false nearest neighbors; specifically, we use a threshold R for the ratio between two distances $D_{\tau,e+1}(t)/D_{\tau,e}(t)$ to determine false nearest neighbors. In the main text, we determine embedding dimension based as the first dimension without any false nearest neighbors for $R = 10$. In Supplementary Materials, we impose $R = 5$ to select for higher dimensions. Once we determine the embedding lag τ and dimension M , we apply the embedding to the entire time series and calculate the nearest neighbor distance against the attractor $A_{\tau,M}$ to obtain a time series of distance from attractor $D_{\tau,M}(t)$.

From a time series of distance from attractor, we estimate pathogen resilience by fitting a linear regression to an appropriate window. To automatically select the fitting window, we begin by smoothing the distance time series using locally estimated scatterplot smoothing (LOESS) to obtain $\hat{D}_{\tau,M}(t)$, where the smoothing is performed on a log scale and exponentiated afterwards. Then, we determine threshold values (T_{start} and T_{end}) for the smoothed distances and choose the fitting window based on when $\hat{D}_{\tau,M}(t)$ crosses these threshold values for the first time. These thresholds are determined by first calculating maximum distance,

$$\max \hat{D} = \max \hat{D}_{\tau,M}(t), \quad (3)$$

and mean pre-pandemic distance,

$$\hat{D}_{\text{mean}} = \frac{1}{N_{t < 2020}} \sum_{t < 2020} \hat{D}_{\tau,M}(t), \quad (4)$$

as a reference, and then dividing their ratios into 10 equal bins:

$$T_{\text{start}} = \hat{D}_{\text{mean}} \times \left(\frac{\max \hat{D}}{\hat{D}_{\text{mean}}} \right)^{9/10} \quad (5)$$

$$T_{\text{end}} = \hat{D}_{\text{mean}} \times \left(\frac{\max \hat{D}}{\hat{D}_{\text{mean}}} \right)^{1/10} \quad (6)$$

This allows us to discard the initial period during which the distance increases (from the introduction of intervention measures) and the final period during which the distance plateaus (as the system reaches an attractor). The fitting window is determined based on when the smoothed distance $\hat{D}_{\tau,M}(t)$ crosses these threshold values for the first time; then, we fit a linear regression to logged (unsmoothed) distances $\log D_{\tau,M}(t)$ using that window.

Mathematical modeling

Throughout the paper, we use a series of mathematical models to illustrate the concept of pathogen resilience and to understand the determinants of pathogen resilience.

439 In general, the intrinsic resilience for a given system is given by the largest real part
 440 of the eigenvalues of the linearized system at endemic equilibrium. Here, we focus on
 441 the SIRS model and present the details of other models in Supplementary Materials.
 442 The SIRS (Susceptible-Infected-Recovered-Susceptible) model is the simplest model
 443 that allows for waning of immunity, where recovered (immune) individuals are as-
 444 sumed to become fully susceptible after an average of $1/\delta$ time period. The dynamics
 445 of the SIRS model is described by the following set of differential equations:

$$\frac{dS}{dt} = \mu - \beta(t)SI - \mu S + \delta R \quad (7)$$

$$\frac{dI}{dt} = \beta(t)SI - (\gamma + \mu)I \quad (8)$$

$$\frac{dR}{dt} = \gamma I - (\delta + \mu)R \quad (9)$$

(10)

446 where μ represents the birth/death rate, $\beta(t)$ represents the time-varying trans-
 447 mission rate, and γ represents the recovery rate. The basic reproduction number
 448 $\mathcal{R}_0 = \beta(t)/(\gamma + \mu)$ is defined as the average number of secondary infections caused
 449 by a single infected individual in a fully susceptible population and measures the
 450 intrinsic transmissibility of a pathogen.

451 When we first introduce the idea of pathogen resilience (Figure 2), we impose
 452 sinusoidal changes to the transmission rate to account for seasonal transmission:

$$\beta(t) = b_1(1 + \theta \cos(2\pi(t - \phi)))\alpha(t), \quad (11)$$

453 where b_1 represents the baseline transmission rate, θ represents the seasonal ampli-
 454 tude, and ϕ represents the seasonal offset term. Here, we also introduce an extra
 455 multiplicative term $\alpha(t)$ to account for the impact of COVID-19 interventions, where
 456 $\alpha(t) < 1$ indicates transmission reduction. Figure 2A and 2B are generated assuming
 457 $b_1 = 3 \times (365/7 + 1/50)/\text{years}$, $\theta = 0.2$, $\phi = 0$, $\mu = 1/50/\text{years}$, $\gamma = 365/7/\text{years}$, and
 458 $\delta = 1/2/\text{years}$. In Figure 2A, we impose a 50% transmission reduction for 6 months
 459 from 2020:

$$\alpha(t) = \begin{cases} 0.5 & 2020 \leq t < 2020.5 \\ 1 & \text{otherwise} \end{cases} \quad (12)$$

460 In Figure 2B, we impose a 50% transmission reduction for 6 months from 2020 and
 461 a permanent 10% reduction onward:

$$\alpha(t) = \begin{cases} 1 & t < 2020 \\ 0.5 & 2020 \leq t < 2020.5 \\ 0.9 & 2020.5 \leq t \end{cases} \quad (13)$$

462 In both scenarios, we simulate the SIRS model from the following initial conditions
 463 ($S(0) = 1/\mathcal{R}_0$, $I(0) = 1 \times 10^{-6}$, and $R(0) = 1 - S(0) - I(0)$) from 1900 until 2030.

464 To measure the empirical resilience of the SIR model (Figure 2C and 2F), we
 465 compute the normalized distance between post-intervention susceptible and logged
 466 infected proportions and their corresponding pre-intervention values at the same time
 467 of year:

$$\sqrt{\left(\frac{S(t) - S_{\text{pre}}(t)}{\sigma_S}\right)^2 + \left(\frac{\log I(t) - \log I_{\text{pre}}(t)}{\sigma_{\log I}}\right)^2}, \quad (14)$$

468 where σ_S and $\sigma_{\log I}$ represent the standard deviation in the pre-intervention suscep-
 469 tible and logged infected proportions. We normalize the differences in susceptible
 470 and logged infected proportions to allow both quantities to equally contribute to the
 471 changes in distance from attractor. In Supplementary Materials, we also compare
 472 the how the degree of seasonal transmission affects empirical resilience by varying
 473 θ from 0 to 0.4; when we assume no seasonality ($\theta = 0$), we do not normalize the
 474 distance because the standard deviation of pre-intervention dynamics are zero.

475 Finally, we use the SIRS model to understand how underlying epidemiological
 476 parameters affect pathogen resilience and link this relationship to underlying sus-
 477 ceptible host dynamics. For the simple SIRS model without seasonal transmission
 478 ($\theta = 0$), the intrinsic resilience corresponds to:

$$-\frac{\text{Re}(\lambda)}{2} = \frac{\delta + \beta I^* + \mu}{2}. \quad (15)$$

479 Here, I^* represents the prevalence values at endemic equilibrium:

$$I^* = \frac{(\delta + \mu)(\beta - (\gamma + \mu))}{\beta(\delta + \gamma + \mu)}. \quad (16)$$

480 The susceptible replenishment rate is given by:

$$S_{\text{replenish}} = \frac{\mu + \delta R}{S^*}, \quad (17)$$

481 where $S^* = 1/\mathcal{R}_0$ represents the equilibrium proportion of susceptible individuals.
 482 We vary the basic reproduction number \mathcal{R}_0 between 1.1 to 6 and the average duration
 483 of immunity $1/\delta$ between 2 to 80 years, and compute these two quantities. In doing
 484 so, we fix all other parameters: $\mu = 1/80/\text{years}$ and $\gamma = 365/7/\text{years}$.

485 **Supplementary Text**

486 **Resilience of a stage-structured system.**

487 In Figure 2G–I, we use a more realistic, stage-structured model to illustrate how
 488 transient phenomena can cause the system to slow down. Specifically, we use the
 489 stage-structured RSV model proposed by [22], which assumes that subsequent rein-
 490 fections cause an individual to become less susceptible and transmissible than previ-
 491 ous infections. The model dynamics can be described as follows:

$$\frac{dM}{dt} = \mu - (\omega + \mu)M \quad (S1)$$

$$\frac{dS_0}{dt} = \omega M - (\lambda(t) + \mu)S_0 \quad (S2)$$

$$\frac{dI_1}{dt} = \lambda(t)S_0 - (\gamma_1 + \mu)I_1 \quad (S3)$$

$$\frac{dS_1}{dt} = \gamma_1 I_1 - (\sigma_1 \lambda(t) + \mu)S_1 \quad (S4)$$

$$\frac{dI_2}{dt} = \sigma_1 \lambda(t)S_1 - (\gamma_2 + \mu)I_2 \quad (S5)$$

$$\frac{dS_2}{dt} = \gamma_2 I_2 - (\sigma_2 \lambda(t) + \mu)S_2 \quad (S6)$$

$$\frac{dI_3}{dt} = \sigma_2 \lambda(t)S_2 - (\gamma_3 + \mu)I_3 \quad (S7)$$

$$\frac{dS_3}{dt} = \gamma_3 I_3 - (\sigma_3 \lambda(t) + \mu)S_3 + \gamma_4 I_4 \quad (S8)$$

$$\frac{dI_4}{dt} = \sigma_3 \lambda(t)S_3 - (\gamma_4 + \mu)I_4 \quad (S9)$$

(S10)

492 where M represents the proportion of individuals who are maternally immune; S_i
 493 represents the proportion of individuals who are susceptible after i prior infections; I_i
 494 represents the proportion of individuals who are currently (re)-infected with their i -th
 495 infection; μ represents the birth and death rates; $1/\omega$ represents the mean duration
 496 of maternal immunity; $1/\gamma_i$ represents the mean duration of infection; $\lambda(t)$ represents
 497 the force of infection; and σ_i represents the reduction in susceptibility for reinfection.
 498 The force of infection is modeled using a sinusoidal function:

$$\beta(t) = b_1(1 + \theta \cos(2\pi(t - \phi)))\alpha(t) \quad (S11)$$

$$\lambda(t) = \beta(I_1 + \rho_1 I_2 + \rho_2(I_3 + I_4)), \quad (S12)$$

499 where b_1 represents the baseline transmission rate; θ represents the seasonal ampli-
 500 tude; ϕ represents the seasonal offset term; $\alpha(t)$ represents the intervention effect;
 501 and ρ_i represents the impact of immunity on transmission reduction. We use the

502 following parameters to simulate the impact of interventions on epidemic dynam-
 503 ics [22]: $b_1 = 9 \times (365/10 + 1/80)/\text{years}$, $\theta = 0.2$, $\phi = -0.1$, $\omega = 365/112/\text{years}$,
 504 $\gamma_1 = 365/10/\text{years}$, $\gamma_2 = 365/7/\text{years}$, $\gamma_3 = 365/5/\text{years}$, $\sigma_1 = 0.76$, $\sigma_2 = 0.6$,
 505 $\sigma_3 = 0.4$, $\rho_1 = 0.75$, $\rho_2 = 0.51$, and $\mu = 1/80/\text{years}$. We assume a 50% transmission
 506 reduction for 6 months from 2020:

$$\alpha(t) = \begin{cases} 0.5 & 2020 \leq t < 2020.5 \\ 1 & \text{otherwise} \end{cases} \quad (\text{S13})$$

507 The model is simulated from 1900 to 2030 using the following initial conditions:
 508 $M = 0$, $S_0 = 1/\mathcal{R}_0 - I_1$, $I_1 = 1 \times 10^{-6}$, $S_1 = 1 - 1/\mathcal{R}_0$, $I_2 = 0$, $S_2 = 0$, $I_3 = 0$,
 509 $S_3 = 0$, and $I_4 = 0$. For the phase plane analysis (Figure 2H) and distance analysis
 510 (Figure 2I), we rely on the average susceptibility,

$$\bar{S} = S_0 + \sigma_1 S_1 + \sigma_2 S_2 + \sigma_3 S_3, \quad (\text{S14})$$

511 and total prevalence,

$$I_{\text{total}} = I_1 + I_2 + I_3 + I_4. \quad (\text{S15})$$

512 These quantities are used to compute the normalized distance from the attractor, as
 513 described in the main text.

514 Resilience of a multistrain system.

515 We use a simple two-strain model to show that a multistrain host-pathogen system
 516 that is coupled through cross immunity can be described by a single resilience value.
 517 The model dynamics can be described as follows [20]:

$$\frac{dS}{dt} = \mu - \mu S - (\lambda_1 + \lambda_2)S + \rho_1 R_1 + \rho_2 R_2 \quad (\text{S16})$$

$$\frac{dI_1}{dt} = \lambda_1 S - (\gamma_1 + \mu)I_1 \quad (\text{S17})$$

$$\frac{dI_2}{dt} = \lambda_2 S - (\gamma_2 + \mu)I_2 \quad (\text{S18})$$

$$\frac{dR_1}{dt} = \gamma_1 I_1 - \lambda_2 \epsilon_{21} R_1 - \rho_1 R_1 + \rho_2 R - \mu R_1 \quad (\text{S19})$$

$$\frac{dR_2}{dt} = \gamma_2 I_2 - \lambda_1 \epsilon_{12} R_2 - \rho_2 R_2 + \rho_1 R - \mu R_2 \quad (\text{S20})$$

$$\frac{dJ_1}{dt} = \lambda_1 \epsilon_{12} R_2 - (\gamma_1 + \mu) J_1 \quad (\text{S21})$$

$$\frac{dJ_2}{dt} = \lambda_2 \epsilon_{21} R_1 - (\gamma_2 + \mu) J_2 \quad (\text{S22})$$

$$\frac{dR}{dt} = \gamma_1 J_1 + \gamma_2 J_2 - \rho_1 R - \rho_2 R - \mu R \quad (\text{S23})$$

518 where S represents the proportion of individuals who are fully susceptible to infections
 519 by both strains; I_1 represents the proportion of individuals who are infected
 520 with strain 1 without prior immunity; I_2 represents the proportion of individuals who
 521 are infected with strain 2 without prior immunity; R_1 represents the proportion of
 522 individuals who are fully immune against strain 1 and partially susceptible to rein-
 523 fection by strain 2; R_2 represents the proportion of individuals who are fully immune
 524 against strain 2 and partially susceptible to reinfection by strain 1; J_1 represents the
 525 proportion of individuals who are infected with strain 1 with prior immunity against
 526 strain 2; J_2 represents the proportion of individuals who are infected with strain
 527 2 with prior immunity against strain 1; R represents the proportion of individuals
 528 who are immune to infections from both strains; μ represents the birth/death rate;
 529 λ_1 and λ_2 represent the force of infection from strains 1 and 2, respectively; ρ_1 and
 530 ρ_2 represent the waning immunity rate; γ_1 and γ_2 represent the recovery rate; ϵ_{12}
 531 and ϵ_{21} represent the susceptibility to reinfection with strains 2 and 1, respectively,
 532 given prior immunity from infection with strains 1 and 2, respectively. The force of
 533 infection is modeled as follows:

$$\beta_1 = b_1(1 + \theta_1 \sin(2\pi(t - \phi_1)))\alpha(t) \quad (\text{S24})$$

$$\beta_2 = b_2(1 + \theta_2 \sin(2\pi(t - \phi_2)))\alpha(t) \quad (\text{S25})$$

$$\lambda_1 = \beta_1(I_1 + J_1) \quad (\text{S26})$$

$$\lambda_2 = \beta_2(I_2 + J_2) \quad (\text{S27})$$

534 In Supplementary Figures S2–S4, we assume the following parameters: $b_1 = 2 \times$
 535 52/years, $b_2 = 4 \times 52/\text{years}$, $\phi_1 = \phi_2 = 0$, $\epsilon_{12} = 0.9$, $\epsilon_{21} = 0.5$, $\gamma_1 = \gamma_2 = 52/\text{years}$,
 536 $\rho_1 = \rho_2 = 1/\text{years}$, and $\mu = 1/70/\text{years}$. For all simulations, we assume a 50%
 537 transmission reduction for 6 months from 2020:

$$\alpha(t) = \begin{cases} 0.5 & 2020 \leq t < 2020.5 \\ 1 & \text{otherwise} \end{cases} \quad (\text{S28})$$

538 The seasonal amplitude θ is varied from 0 to 0.4. All simulations are ran from 1900
 539 to 2030 from the following initial conditions: $S(0) = 1 - 2 \times 10^{-6}$, $I_1(0) = 1 \times 10^{-6}$,
 540 $I_2(0) = 1 \times 10^{-6}$, $R_1(0) = 0$, $R_2(0) = 0$, $J_1(0) = 0$, $J_2(0) = 0$, and $R(0) = 0$.

541 For this, we consider three different scenarios for measuring pathogen resilience:
 542 (1) we only have information about strain 1, (2) we only have information about
 543 strain 2, and (3) we are unable to distinguish the differences between strains. In
 544 the first two scenarios (see panels A–C for strain 1 and panels D–F for strain 2), we
 545 consider the dynamics of average susceptibility for each strain and total prevalence:

$$\bar{S}_1 = S + \epsilon_{12}R_2 \quad (\text{S29})$$

$$\hat{I}_1 = I_1 + J_1 \quad (\text{S30})$$

$$\bar{S}_2 = S + \epsilon_{21}R_1 \quad (\text{S31})$$

$$\hat{I}_2 = I_2 + J_2 \quad (\text{S32})$$

⁵⁴⁶ In the third scenario (panels G–I), we consider the dynamics of total susceptible and
⁵⁴⁷ infected population:

$$\hat{S} = S + R_2 + R_1 \quad (\text{S33})$$

$$\hat{I} = I_1 + J_1 + I_2 + J_2 \quad (\text{S34})$$

$$(\text{S35})$$

⁵⁴⁸ These quantities are used to compute the normalized distance from the attractor, as
⁵⁴⁹ described in the main text.

⁵⁵⁰ Estimating intrinsic resilience using mechanistic model

⁵⁵¹ We test whether we can reliably estimate the intrinsic resilience of a system by fitting
⁵⁵² a mechanistic model. Specifically, we simulate case time series from stochastic SIRS
⁵⁵³ and two-strain models and fit a simple, deterministic SIRS model using a Bayesian
⁵⁵⁴ framework.

⁵⁵⁵ First, we describe the simulation set up. The stochastic SIRS model can be
⁵⁵⁶ written as follows:

$$\beta(t) = \mathcal{R}_0 \left(1 + \theta \cos \left(\frac{2\pi t}{364} \right) \right) \alpha(t)(1 - \exp(-\gamma)) \quad (\text{S36})$$

$$\text{FOI}(t) = \beta(t)I(t - \Delta t)/N \quad (\text{S37})$$

$$B(t) \sim \text{Poisson}(\mu N) \quad (\text{S38})$$

$$\Delta S(t) \sim \text{Binom}(S(t - \Delta t), 1 - \exp(-(\text{FOI}(t) + \mu)\Delta t)) \quad (\text{S39})$$

$$N_{SI}(t) \sim \text{Binom}\left(\Delta S(t), \frac{\text{FOI}(t)}{\text{FOI}(t) + \mu}\right) \quad (\text{S40})$$

$$\Delta I(t) \sim \text{Binom}(I(t - \Delta t), 1 - \exp(-(\gamma + \mu)\Delta t)) \quad (\text{S41})$$

$$N_{IR}(t) \sim \text{Binom}\left(\Delta I(t), \frac{\gamma}{\gamma + \mu}\right) \quad (\text{S42})$$

$$\Delta R(t) \sim \text{Binom}(R(t - \Delta t), 1 - \exp(-(\delta + \mu)\Delta t)) \quad (\text{S43})$$

$$N_{RS}(t) \sim \text{Binom}\left(\Delta R(t), \frac{\delta}{\delta + \mu}\right) \quad (\text{S44})$$

$$S(t) = S(t - \Delta t) + N_{RS}(t) + B(t) - \Delta S(t) \quad (\text{S45})$$

$$I(t) = I(t - \Delta t) + N_{SI}(t) - \Delta I(t) \quad (\text{S46})$$

$$R(t) = R(t - \Delta t) + N_{IR}(t) - \Delta R(t) \quad (\text{S47})$$

⁵⁵⁷ where FOI represent the force of infection; N_{ij} represent the number of individuals
⁵⁵⁸ moving from compartment i to j on a given day; and $B(t)$ represents the number
⁵⁵⁹ of new births. We simulate the model on a daily scale—assuming 364 days in a
⁵⁶⁰ year so that it can be evenly grouped into 52 weeks—with the following parameters:
⁵⁶¹ $\mathcal{R}_0 = 3$, $\theta = 0.1$, $\gamma = 1/7/\text{days}$, $\delta = 1/(364 \times 2)/\text{days}$, $\mu = 1/(364 \times 50)/\text{days}$, and

562 $N = 1 \times 10^8$. The model is simulated from 1900 to 2030 assuming $S(0) = N/3$,
563 $I(0) = 100$, and $R(0) = N - S(0) - I(0)$. The observed incidence from the model is
564 then simulated as follows:

$$C(t) = \text{Beta} - \text{Binom}(N_{SI}(t), \rho, k), \quad (\text{S48})$$

565 where ρ represents the reporting probability and k represents the overdispersion pa-
566 rameter of beta-binomial distribution. We assume $\rho = 0.002$ (i.e., 0.2% probability)
567 and $k = 1000$.

568 The stochastic two-strain model can be written as follows:

$$\beta_1(t) = b_1 \left(1 + \theta_1 \cos \left(\frac{2\pi(t - \phi_1)}{364} \right) \right) \alpha(t) \quad (\text{S49})$$

$$\beta_2(t) = b_2 \left(1 + \theta_2 \cos \left(\frac{2\pi(t - \phi_2)}{364} \right) \right) \alpha(t) \quad (\text{S50})$$

$$\text{FOI}_1(t) = \beta_1(t)(I_1(t - \Delta t) + J_1(t - \Delta t))/N \quad (\text{S51})$$

$$\text{FOI}_2(t) = \beta_2(t)(I_2(t - \Delta t) + J_2(t - \Delta t))/N \quad (\text{S52})$$

$$B(t) \sim \text{Poisson}(\mu N) \quad (\text{S53})$$

$$\Delta S(t) \sim \text{Binom}(S(t - \Delta t), 1 - \exp(-(\text{FOI}_1(t) + \text{FOI}_2(t) + \mu)\Delta t)) \quad (\text{S54})$$

$$N_{SI_1}(t) \sim \text{Binom}\left(\Delta S(t), \frac{\text{FOI}_1(t)}{\text{FOI}_1(t) + \text{FOI}_2(t) + \mu}\right) \quad (\text{S55})$$

$$N_{SI_2}(t) \sim \text{Binom}\left(\Delta S(t), \frac{\text{FOI}_2(t)}{\text{FOI}_1(t) + \text{FOI}_2(t) + \mu}\right) \quad (\text{S56})$$

$$\Delta I_1(t) \sim \text{Binom}(I_1(t - \Delta t), 1 - \exp(-(\gamma_1 + \mu)\Delta t)) \quad (\text{S57})$$

$$N_{I_1 R_1}(t) \sim \text{Binom}\left(\Delta I_1(t), \frac{\gamma_1}{\gamma_1 + \mu}\right) \quad (\text{S58})$$

$$\Delta I_2(t) \sim \text{Binom}(I_2(t - \Delta t), 1 - \exp(-(\gamma_2 + \mu)\Delta t)) \quad (\text{S59})$$

$$N_{I_2 R_2}(t) \sim \text{Binom}\left(\Delta I_2(t), \frac{\gamma_2}{\gamma_2 + \mu}\right) \quad (\text{S60})$$

$$\Delta R_1(t) \sim \text{Binom}(R_1(t - \Delta t), 1 - \exp(-(\epsilon_{21}\text{FOI}_2(t) + \rho_1 + \mu)\Delta t)) \quad (\text{S61})$$

$$N_{R_1 S}(t) \sim \text{Binom}\left(\Delta R_1(t), \frac{\rho_1}{\epsilon_{21}\text{FOI}_2(t) + \rho_1 + \mu}\right) \quad (\text{S62})$$

$$N_{R_1 J_2}(t) \sim \text{Binom}\left(\Delta R_1(t), \frac{\epsilon_{21}\text{FOI}_2(t)}{\epsilon_{21}\text{FOI}_2(t) + \rho_1 + \mu}\right) \quad (\text{S63})$$

$$\Delta R_2(t) \sim \text{Binom}(R_2(t - \Delta t), 1 - \exp(-(\epsilon_{12}\text{FOI}_1(t) + \rho_2 + \mu)\Delta t)) \quad (\text{S64})$$

$$N_{R_2 S}(t) \sim \text{Binom}\left(\Delta R_2(t), \frac{\rho_2}{\epsilon_{12}\text{FOI}_1(t) + \rho_2 + \mu}\right) \quad (\text{S65})$$

$$N_{R_2 J_1}(t) \sim \text{Binom}\left(\Delta R_2(t), \frac{\epsilon_{12}\text{FOI}_1(t)}{\epsilon_{12}\text{FOI}_1(t) + \rho_2 + \mu}\right) \quad (\text{S66})$$

$$\Delta J_1(t) \sim \text{Binom}(J_1(t - \Delta t), 1 - \exp(-(\gamma_1 + \mu)\Delta t)) \quad (\text{S67})$$

$$N_{J_1R}(t) \sim \text{Binom}\left(\Delta J_1(t), \frac{\gamma_1}{\gamma_1 + \mu}\right) \quad (\text{S68})$$

$$\Delta J_2(t) \sim \text{Binom}(J_2(t - \Delta t), 1 - \exp(-(\gamma_2 + \mu)\Delta t)) \quad (\text{S69})$$

$$N_{J_2R}(t) \sim \text{Binom}\left(\Delta J_2(t), \frac{\gamma_2}{\gamma_2 + \mu}\right) \quad (\text{S70})$$

$$\Delta R(t) \sim \text{Binom}(R(t - \Delta t), 1 - \exp(-(\rho_1 + \rho_2 + \mu)\Delta t)) \quad (\text{S71})$$

$$N_{RR_1}(t) \sim \text{Binom}\left(\Delta R(t), \frac{\rho_1}{\rho_1 + \rho_2 + \mu}\right) \quad (\text{S72})$$

$$N_{RR_2}(t) \sim \text{Binom}\left(\Delta R(t), \frac{\rho_2}{\rho_1 + \rho_2 + \mu}\right) \quad (\text{S73})$$

$$S(t) = S(t - \Delta t) - \Delta S(t) + B(t) + N_{R_1S}(t) + N_{R_2S}(t) \quad (\text{S74})$$

$$I_1(t) = I_1(t - \Delta t) - \Delta I_1(t) + N_{SI_1}(t) \quad (\text{S75})$$

$$I_2(t) = I_2(t - \Delta t) - \Delta I_2(t) + N_{SI_2}(t) \quad (\text{S76})$$

$$R_1(t) = R_1(t - \Delta t) - \Delta R_1(t) + N_{I_1R_1}(t) + N_{RR_1}(t) \quad (\text{S77})$$

$$R_2(t) = R_2(t - \Delta t) - \Delta R_2(t) + N_{I_2R_2}(t) + N_{RR_2}(t) \quad (\text{S78})$$

$$J_1(t) = J_1(t - \Delta t) - \Delta J_1(t) + N_{R_2J_1}(t) \quad (\text{S79})$$

$$J_2(t) = J_2(t - \Delta t) - \Delta J_2(t) + N_{R_1J_2}(t) \quad (\text{S80})$$

$$R(t) = R(t - \Delta t) - \Delta R(t) + N_{J_1R}(t) + N_{J_2R}(t) \quad (\text{S81})$$

569 We simulate the model on a daily scale with previously estimated parameters for the
 570 RSV-HMPV interaction [20]: $b_1 = 1.7/\text{weeks}$, $b_2 = 1.95/\text{weeks}$, $\theta_1 = 0.4$, $\theta_2 = 0.3$,
 571 $\phi_1 = 0.005 \times 7/364$, $\phi_2 = 4.99 \times 7/364$, $\epsilon_{12} = 0.92$, $\epsilon_{21} = 0.45$, $\gamma_1 = 1/10/\text{days}$,
 572 $\gamma_2 = 1/10/\text{days}$, $\rho_1 = 1/364/\text{days}$, $\rho_2 = 1/364/\text{days}$, $\mu = 1/(70 \times 364)/\text{days}$, and
 573 $N = 1 \times 10^8$. The model is simulated from 1900 to 2030 assuming $S(0) = N - 200$,
 574 $I_1(0) = 100$, $I_2(0) = 100$, $R_1(0) = 0$, $R_2(0) = 0$, $J_1(0) = 0$, $J_2(0) = 0$, and $R(0) = 0$.
 575 The observed incidence for each strain is then simulated as follows:

$$C_1(t) = \text{Beta} - \text{Binom}(N_{SI_1}(t) + N_{R_2J_1}, \rho, k), \quad (\text{S82})$$

$$C_2(t) = \text{Beta} - \text{Binom}(N_{SI_2}(t) + N_{R_1J_2}, \rho, k), \quad (\text{S83})$$

576 where ρ represents the reporting probability and k represents the overdispersion pa-
 577 rameter of beta-binomial distribution. We assume $\rho = 0.002$ (i.e., 0.2% probability)
 578 and $k = 500$. We also consider the total incidence: $C_{\text{total}}(t) = C_1(t) + C_2(t)$.

579 For both models, we consider a more realistic challenges in intervention effects
 580 $\alpha(t)$ to challenge our ability to estimate the intervention effects. Thus, we assume
 581 a 40% transmission reduction for 3 months from March 2020, followed by a 10%
 582 transmission reduction for 6 months, 20% transmission reduction for 3 months, and

583 a final return to normal levels:

$$\alpha(t) = \begin{cases} 1 & t < 2020.25 \\ 0.6 & 2020.25 \leq t < 2020.5 \\ 0.9 & 2020.5 \leq t < 2021 \\ 0.8 & 2021 \leq t < 2021.25 \\ 1 & 2021.25 \leq t \end{cases}. \quad (\text{S84})$$

584 For all simulations, we truncate the time series from the beginning of 2014 to the
585 end of 2023 and aggregate them into weekly cases.

586 To infer intrinsic resilience from time series, we fit a simple discrete time, deter-
587 ministic SIRS model [4]:

$$\Delta t = 1 \text{ week} \quad (\text{S85})$$

$$\text{FOI}(t) = \beta(t)(I(t - \Delta t) + \omega)/N \quad (\text{S86})$$

$$\Delta S(t) = [1 - \exp(-(\text{FOI}(t) + \mu)\Delta t)] S(t - \Delta t) \quad (\text{S87})$$

$$N_{SI}(t) = \frac{\text{FOI}(t)\Delta S(t)}{\text{FOI}(t) + \mu} \quad (\text{S88})$$

$$\Delta I(t) = [1 - \exp(-(\gamma + \mu)\Delta t)] I(t - \Delta t) \quad (\text{S89})$$

$$N_{IR}(t) = \frac{\gamma \Delta I(t)}{\gamma + \mu} \quad (\text{S90})$$

$$\Delta R(t) = [1 - \exp(-(\nu + \mu)\Delta t)] R(t - \Delta t) \quad (\text{S91})$$

$$N_{RS}(t) = \frac{\nu \Delta R(t)}{\nu + \mu} \quad (\text{S92})$$

$$S(t) = S(t - \Delta t) + \mu S - \Delta S(t) + N_{RS}(t) \quad (\text{S93})$$

$$I(t) = I(t - \Delta t) - \Delta I(t) + N_{SI}(t) \quad (\text{S94})$$

$$R(t) = R(t - \Delta t) - \Delta R(t) + N_{IR}(t) \quad (\text{S95})$$

588 where we include an extra term ω to account for external infections. Although actual
589 simulations do not include any external infections, we found that including this term
590 generally helped with model convergence in previous analyses [4]. The transmission
591 rate is divided into a seasonal term $\beta_{\text{seas}}(t)$ (repeated every year) and intervention
592 term $\alpha(t)$, which are estimated jointly:

$$\beta(t) = \beta_{\text{seas}}(t)\alpha(t), \quad (\text{S96})$$

593 where $\alpha < 1$ corresponds to reduction in transmission due to intervention effects. To
594 constrain the smoothness of $\beta_{\text{seas}}(t)$, we impose cyclic, random-walk priors:

$$\beta_{\text{seas}}(t) \sim \text{Normal}(\beta_{\text{seas}}(t - 1), \sigma) \quad t = 2 \dots 52 \quad (\text{S97})$$

$$\beta_{\text{seas}}(1) \sim \text{Normal}(\beta_{\text{seas}}(52), \sigma) \quad (\text{S98})$$

595 [SWP: I noticed that I forgot to put a prior on σ so need to re-do this but won't
 596 change the results.] We fix $\alpha(t) = 1$ for all $t < 2020$ and estimate α assuming a
 597 normal prior:

$$\alpha \sim \text{Normal}(1, 0.25). \quad (\text{S99})$$

598 We assume weakly informative priors on ω and τ :

$$\omega \sim \text{Normal}(0, 200) \tau \sim \text{Normal}(104, 26) \quad (\text{S100})$$

599 We assume that the true birth/death rates, population sizes, and recovery rates are
 600 known. We note, however, that assuming $\gamma = 1/\text{week}$ actually correspond to a
 601 mean infectious period of 1.6 weeks, which is much longer than the true value; this
 602 approximation allows us to test whether we can still robustly estimate the intrinsic
 603 resilience given parameters mis-specification. Initial conditions are estimated with
 604 following priors:

$$S(0) = Ns(0) \quad (\text{S101})$$

$$I(0) = Ni(0) \quad (\text{S102})$$

$$s(0) \sim \text{Uniform}(0, 1) \quad (\text{S103})$$

$$i(0) \sim \text{Half-Normal}(0, 0.001) \quad (\text{S104})$$

605 Finally, the Observation model is specified as follows:

$$\text{Cases}(t) \sim \text{Negative-Binomial}(\rho N_{SI}(t), \phi) \quad (\text{S105})$$

$$\rho \sim \text{Half-Normal}(0, 0.02) \quad (\text{S106})$$

$$\phi \sim \text{Half-Normal}(0, 10) \quad (\text{S107})$$

606 where ρ represents the reporting probability and ϕ represents the negative binomial
 607 overdispersion parameter.

608 The model is fitted to four separate time series: (1) incidence time series from
 609 the SIRS model, (2) incidence time series for strain 1 from the two-strain model,
 610 (3) incidence time series for strain 2 from the two-strain model, and (4) combined
 611 incidence time series for strains 1 and 2 from the two-strain model. The model was
 612 fitted using rstan [27, 28]. The resulting posterior distribution was used to calculate
 613 the intrinsic resilience of the seasonally unforced system with the same parameters;
 614 eigenvalues of the discrete-time SIR model were computed by numerically finding
 615 the equilibrium and calculating the Jacobian matrix.

616 **Validations for window-selection criteria**

617 We use stochastic SIRS simulations to validate the window-selection criteria that we
 618 use for the linear regression for estimating empirical resilience. For each simulation,
 619 we begin by generating a random intervention $\alpha(t)$ from random set of parameters.
 620 First, we draw the duration of intervention τ_{np}^* from a uniform distribution between

621 0.5 and 3.5 years. Then, we draw independent normal variables z_i of length $\lfloor 364\tau_{\text{npi}} \rfloor$
622 with a standard deviation of 0.02 and take a reverse cumulative sum to obtain a
623 realistic shape for the intervention:

$$x_n = 1 + \sum_{i=n}^{\lfloor 364\tau_{\text{npi}} \rfloor} z_i, \quad n = 1, \dots, \lfloor 364\tau_{\text{npi}} \rfloor. \quad (\text{S108})$$

624 We repeat this random generation process until less than 10% of x_n exceeds 1. Then,
625 we set any values that are above 1 or below 0 as 1 and 0, respectively. Then, we
626 randomly draw the minimum transmission during intervention α_{\min} from a uniform
627 distribution between 0.5 and 0.7 and scale x_n to have a minimum of α_{\min} :

$$x_{\text{scale},n} = \alpha_{\min} + (1 - \alpha_{\min}) \times \frac{x_n - \min x_n}{1 - \min x_n}. \quad (\text{S109})$$

628 This allows us to simulate a realistically shaped interventions:

$$\alpha(t) = \begin{cases} 1 & t < 2020 \\ x_{\text{scale},364(t-2020)} & 2020 \leq t < 2020 + \tau_{\text{npi}} \\ 1 & \tau_{\text{npi}} \leq t \end{cases}. \quad (\text{S110})$$

629 Given this intervention function, we draw \mathcal{R}_0 from a uniform distribution between 1.5
630 and 3 and the mean duration of immunity $1/\delta$ from a uniform distribution between
631 0.5 and 2. Then, we simulate the stochastic SIRS model from $S(0) = 10^8/\mathcal{R}_0$ and
632 $I(0) = 100$ from 1990 to 2025 and truncate the time series to 2014–2025; if the
633 epidemic becomes extinct before the end of simulation, we discard that simulation
634 and start over from the intervention generation step. We then apply the window
635 selection criteria described in the main text to compute the empirical resilience and
636 compare it against the intrinsic resilience of the seasonally unforced system. We also
637 compare this with the naive approach that uses the entire distance-from-attractor
638 time series, starting from the maximum distance. We repeat this procedure 500
639 times and quantify the correlation between empirical and intrinsic resilience estimates
640 across two approaches.

Supplementary Figures

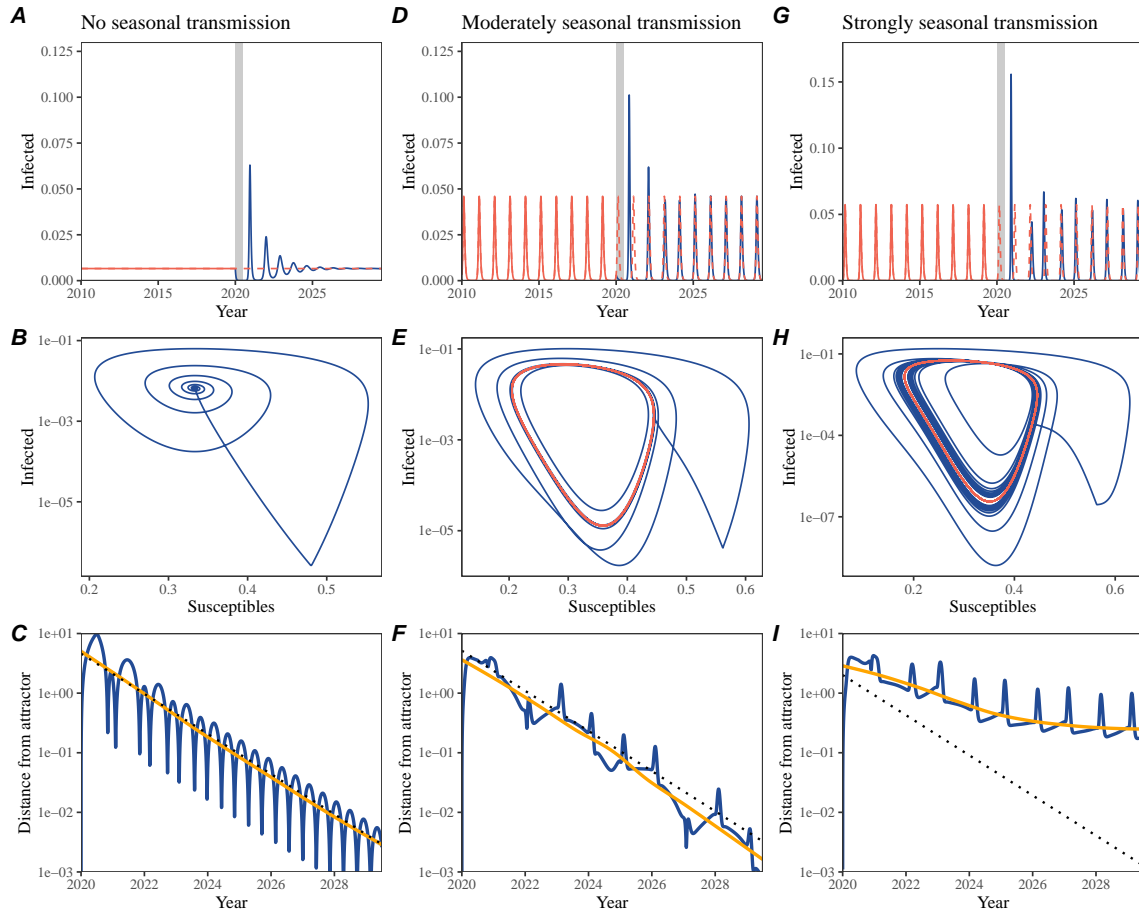


Figure S1: Impact of seasonal transmission on pathogen resilience. (A, D, G) Simulated epidemic trajectories using the SIRS model without seasonal forcing (A), with seasonal forcing of amplitude of 0.2 (D), and with seasonal forcing of amplitude of 0.2 (G). Red and blue solid lines represent epidemic dynamics before and after interventions are introduced, respectively. Red dashed lines represent counterfactual epidemic dynamics in the absence of interventions. Gray regions indicate the duration of interventions. (B, E, H) Phase plane representation of the corresponding model. Red and blue solid lines represent epidemic trajectories on an SI phase plane before and after interventions are introduced, respectively. (C, F, I) Changes in logged distance from attractor over time. Blue lines represent the logged distance from attractor. Orange lines represent the locally estimated scatterplot smoothing (LOESS) fits to the logged distance from attractor. Dotted lines are superimposed as a comparison to have the same slope as the intrinsic resilience of the seasonally unforced system.

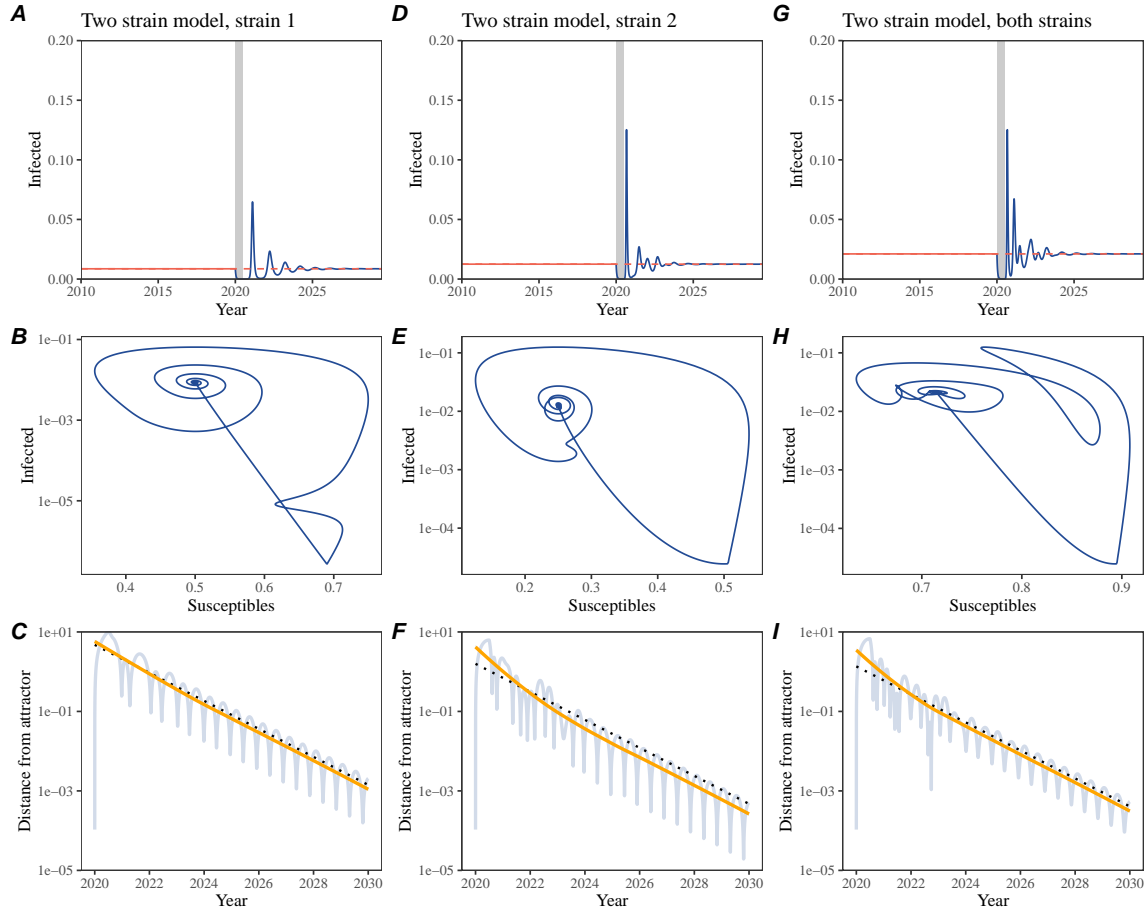


Figure S2: Conceptual framework for measuring pathogen resilience following NPIs for a multi-strain system without seasonal forcing. (A, D, G) Simulated epidemic trajectories using a multi-strain system without seasonal forcing. Red and blue solid lines represent epidemic dynamics before and after interventions are introduced, respectively. Red dashed lines represent counterfactual epidemic dynamics in the absence of interventions. Gray regions indicate the duration of interventions. (B, E, H) Phase plane representation of the corresponding model. Red and blue solid lines represent epidemic trajectories on an SI phase plane before and after interventions are introduced, respectively. (C, F, I) Changes in logged distance from attractor over time. Blue lines represent the logged distance from attractor. Orange lines represent the locally estimated scatterplot smoothing (LOESS) fits to the logged distance from attractor. Dotted lines are superimposed as a comparison to have the same slope as the intrinsic resilience of the seasonally unforced system.

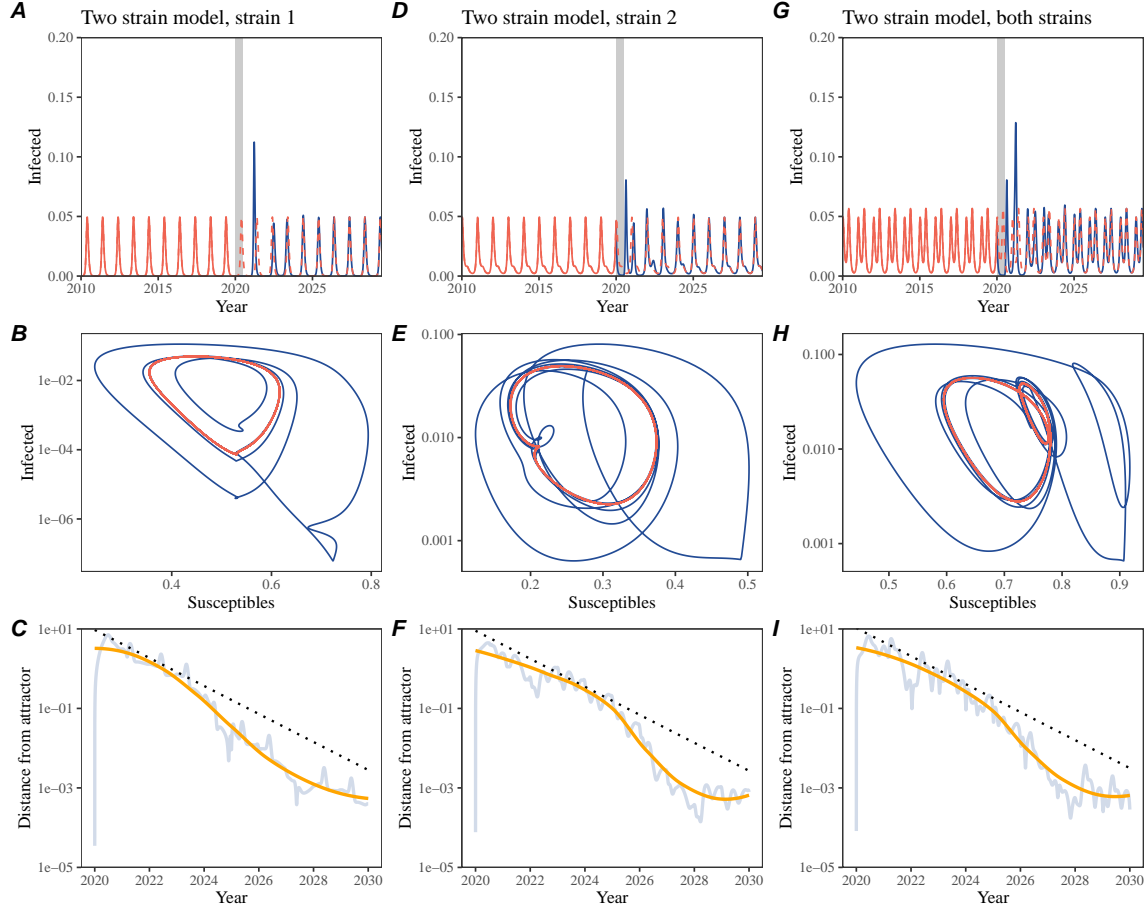


Figure S3: Conceptual framework for measuring pathogen resilience following NPIs for a multi-strain system with seasonal forcing. (A, D, G) Simulated epidemic trajectories using a multi-strain system with seasonal forcing (amplitude of 0.2). Red and blue solid lines represent epidemic dynamics before and after interventions are introduced, respectively. Red dashed lines represent counterfactual epidemic dynamics in the absence of interventions. Gray regions indicate the duration of interventions. (B, E, H) Phase plane representation of the corresponding model. Red and blue solid lines represent epidemic trajectories on an SI phase plane before and after interventions are introduced, respectively. (C, F, I) Changes in logged distance from attractor over time. Blue lines represent the logged distance from attractor. Orange lines represent the locally estimated scatterplot smoothing (LOESS) fits to the logged distance from attractor. Dotted lines are superimposed as a comparison to have the same slope as the intrinsic resilience of the seasonally unforced system.

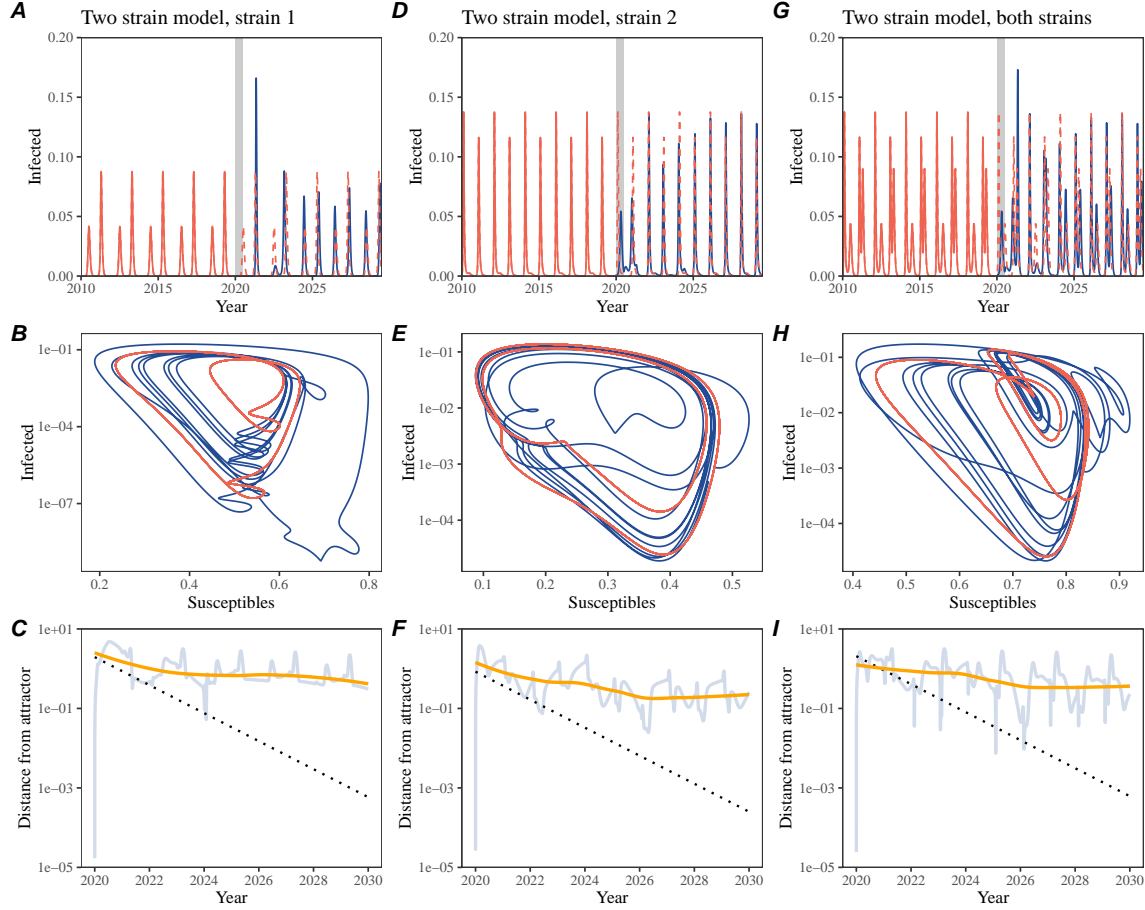


Figure S4: Conceptual framework for measuring pathogen resilience following NPIs for a multi-strain system with strong seasonal forcing. (A, D, G) Simulated epidemic trajectories using a multi-strain system with seasonal forcing (amplitude of 0.4). Red and blue solid lines represent epidemic dynamics before and after interventions are introduced, respectively. Red dashed lines represent counterfactual epidemic dynamics in the absence of interventions. Gray regions indicate the duration of interventions. (B, E, H) Phase plane representation of the corresponding model. Red and blue solid lines represent epidemic trajectories on an SI phase plane before and after interventions are introduced, respectively. (C, F, I) Changes in logged distance from attractor over time. Blue lines represent the logged distance from attractor. Orange lines represent the locally estimated scatterplot smoothing (LOESS) fits to the logged distance from attractor. Dotted lines are superimposed as a comparison to have the same slope as the intrinsic resilience of the seasonally unforced system.

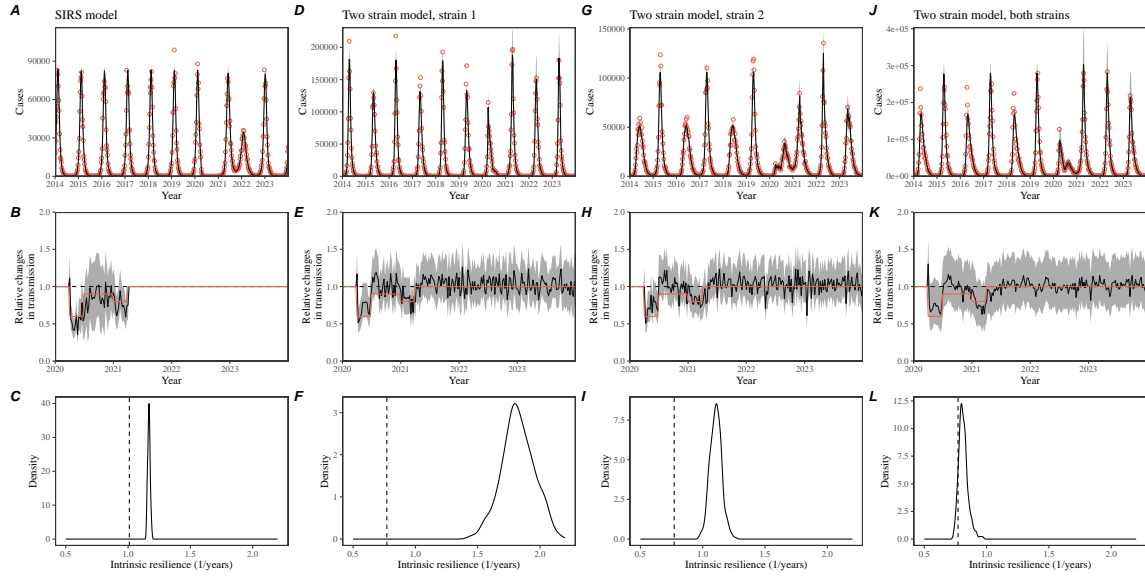


Figure S5: Mechanistic model fits to simulated data and inferred intrinsic resilience. (A, D, G, J) Simulated case time series from corresponding models (red) and SIRS model fits (black). (B, E, H, K) Assumed changes in transmission due to COVID-19 interventions (red) and estimated changes from the SIRS model (black). Solid lines and shaded regions represent fitted posterior median and 95% credible intervals. (C, F, I, L) True intrinsic resilience of the seasonally unforced system (vertical lines) and the posterior distribution of the inferred intrinsic resilience from the SIRS model (density plots).

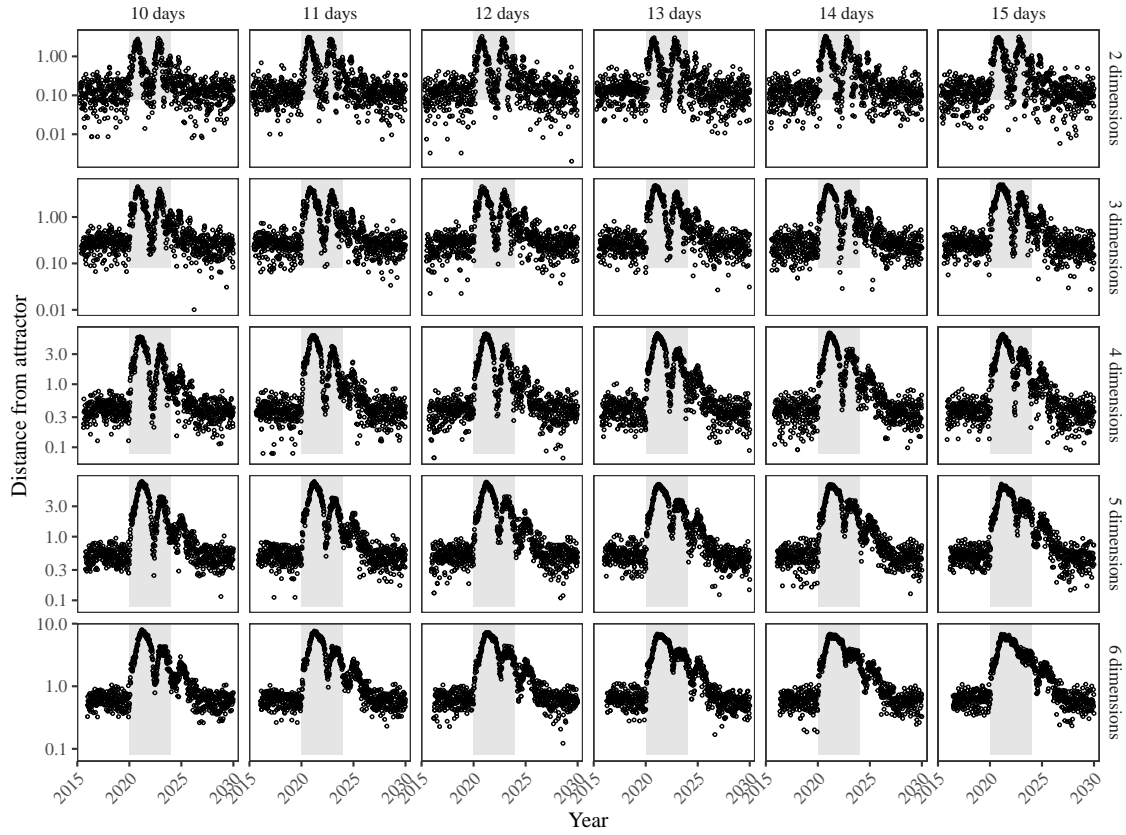


Figure S6: Sensitivity of the distance from attractor to choices about embedding lags and dimensions. Sensitivity analysis for the distance-from-attractor time series shown in Figure 3E in the main text by varying the embedding lag between 10–15 days and embedding dimensions between 2–6 dimensions.

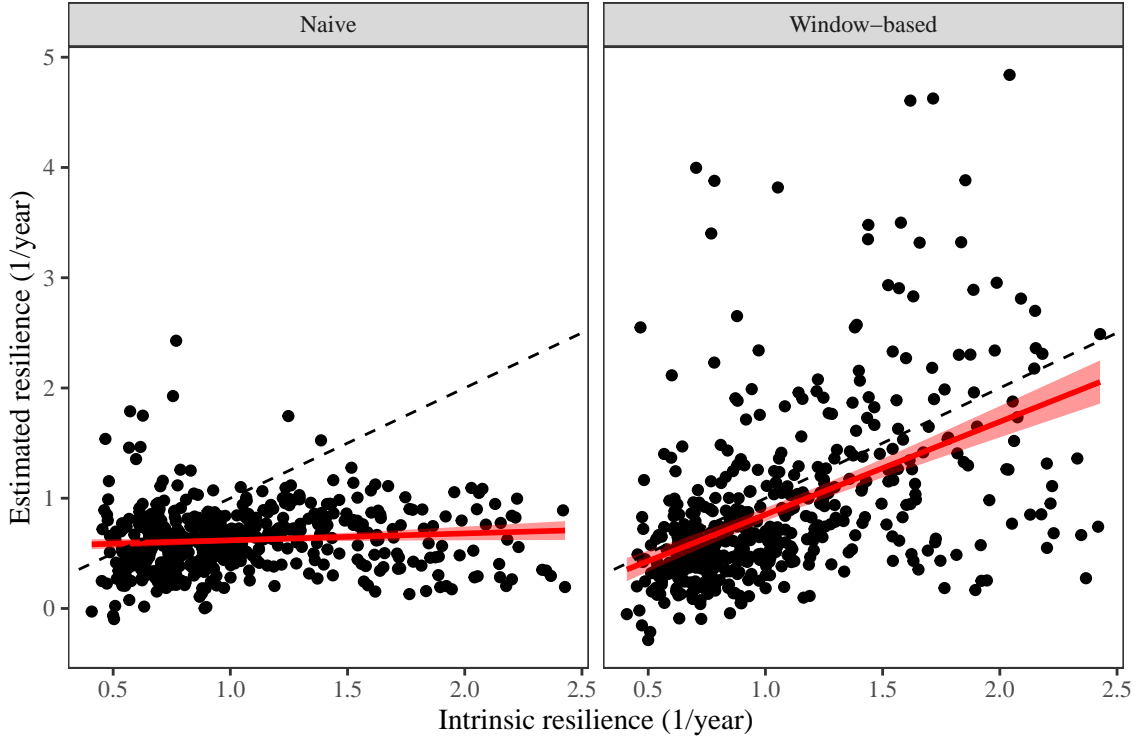


Figure S7: Impact of fitting window selection on the estimation of empirical resilience. We simulate 500 epidemics using stochastic SIRS model with randomly drawn parameters and randomly generated intervention impacts. For each simulation, we reconstruct the empirical attractor based on the approach outlined in Figure 3 and estimate the distance from attractor. The naive approach fits a linear regression on a log scale, starting from the maximum distance until the end of the time series. The window-based approach tries to select an appropriate window by smoothing the distance estimates and finding a time period when the smoothed time series crosses pre-determined threshold, relatively to the maximum distance; then, a linear regression is fitted by using the raw distance within this time period.

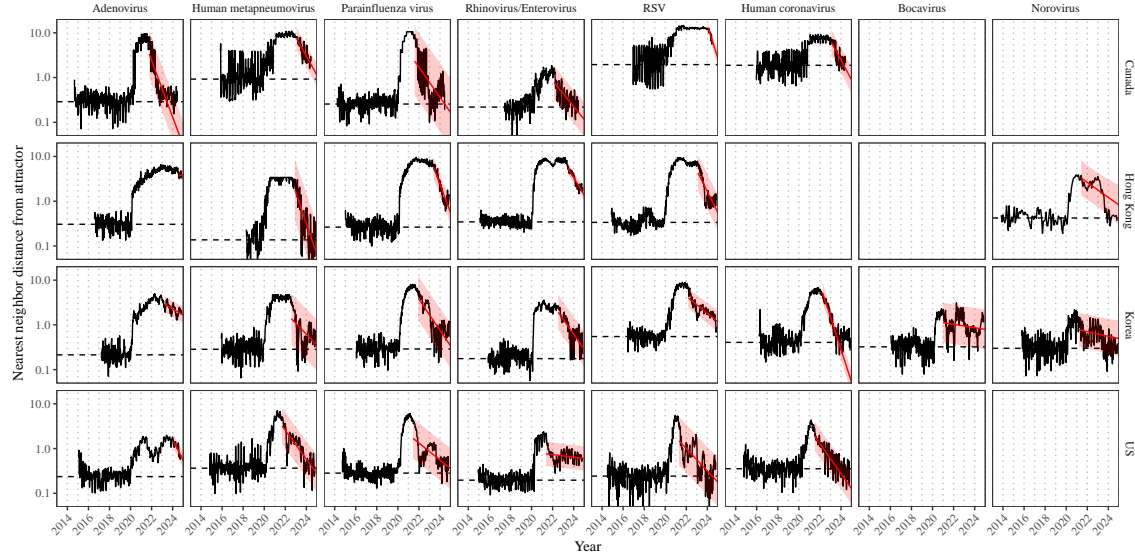


Figure S8: Estimated time series of distance from attractor for each pathogen across Canada, Hong Kong, Korea, and the US. Black lines represent the estimated distance from attractor. Red lines and shaded regions represent the linear regression fits and corresponding 95% confidence intervals. Dashed lines represent the average of the pre-pandemic nearest neighbor distances.

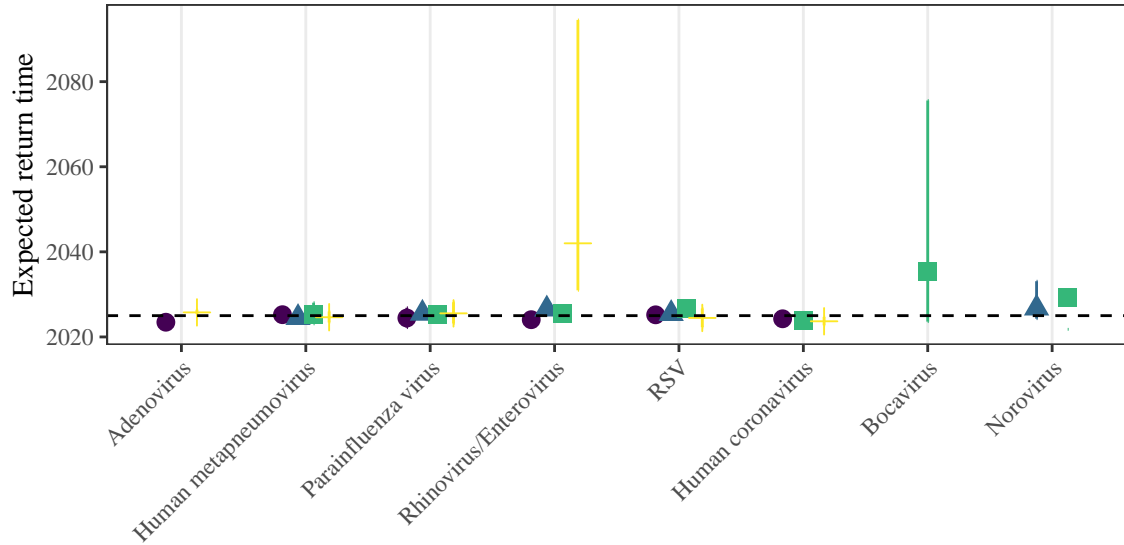


Figure S9: **Predicted timing of when each pathogen will return to their pre-pandemic cycles (zoomed out).** The dashed line in panel B indicates the end of 2024 (current observation time). Error bars represent 95% confidence intervals.

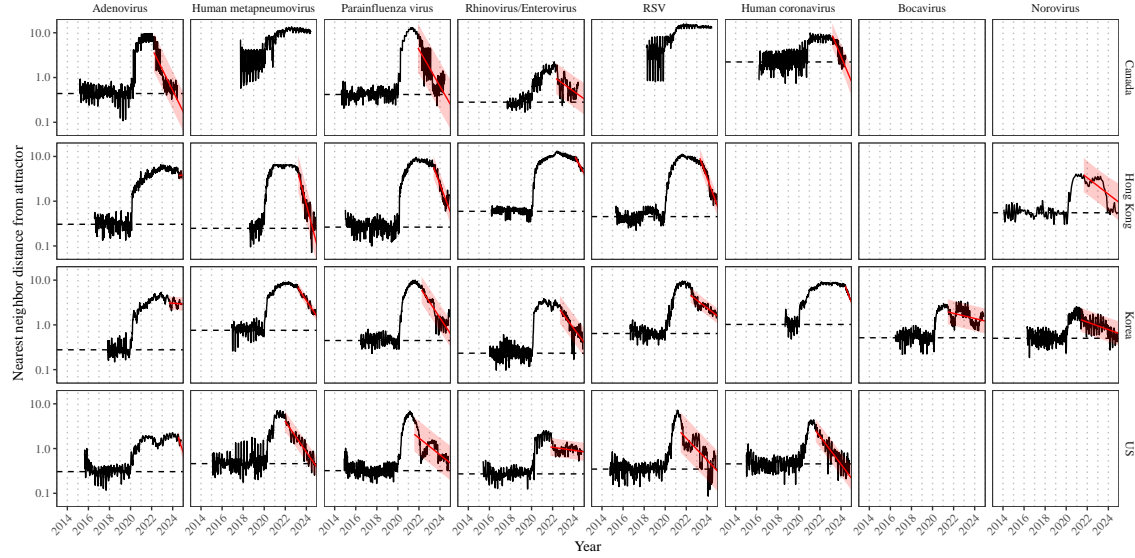


Figure S10: Estimated time series of distance from attractor for each pathogen across Canada, Hong Kong, Korea, and the US using higher embedding dimensions. Black lines represent the estimated distance from attractor. Red lines and shaded regions represent the linear regression fits and corresponding 95% confidence intervals. Dashed lines represent the average of the pre-pandemic nearest neighbor distances. A lower threshold is used for determining embedding dimensions with the false nearest neighbors approach, thereby yielding a higher embedding dimension.

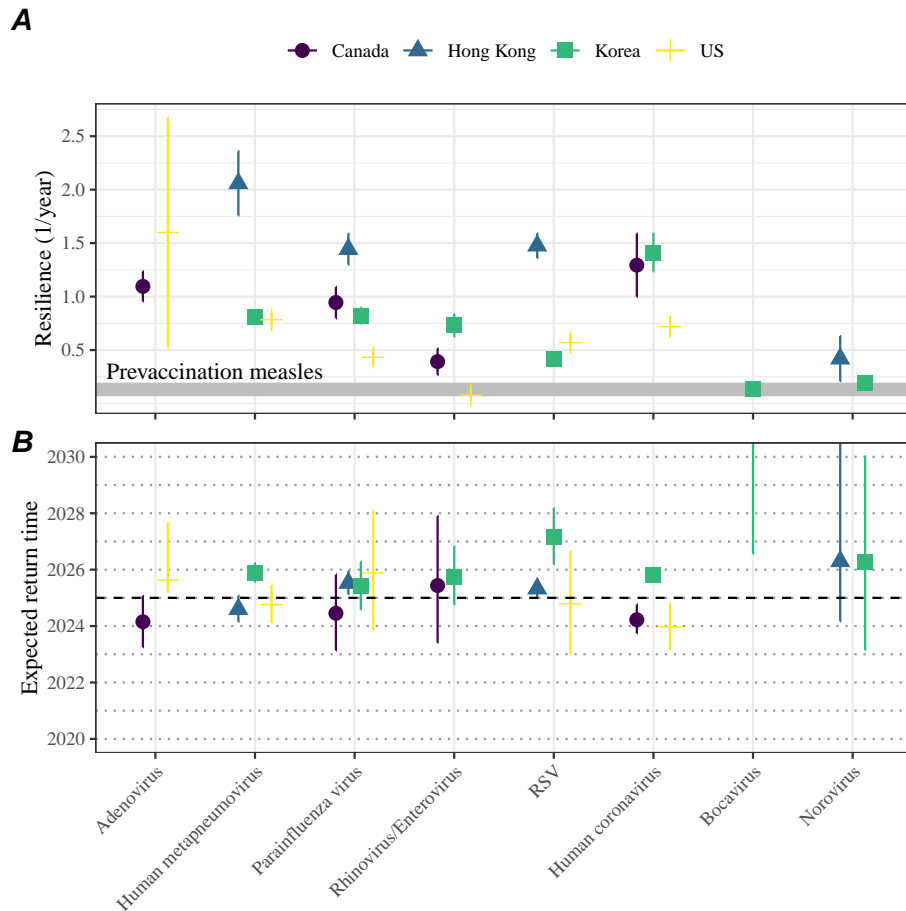


Figure S11: Summary of resilience estimates using higher embedding dimensions. (A) Estimated pathogen resilience. The gray horizontal line represents the intrinsic resilience of pre-vaccination measles dynamics. (B) Predicted timing of when each pathogen will return to their pre-pandemic cycles. The dashed line in panel B indicates the end of 2024 (current observation time). Error bars represent 95% confidence intervals. A lower threshold is used for determining embedding dimensions with the false nearest neighbors approach, thereby yielding a higher embedding dimension.

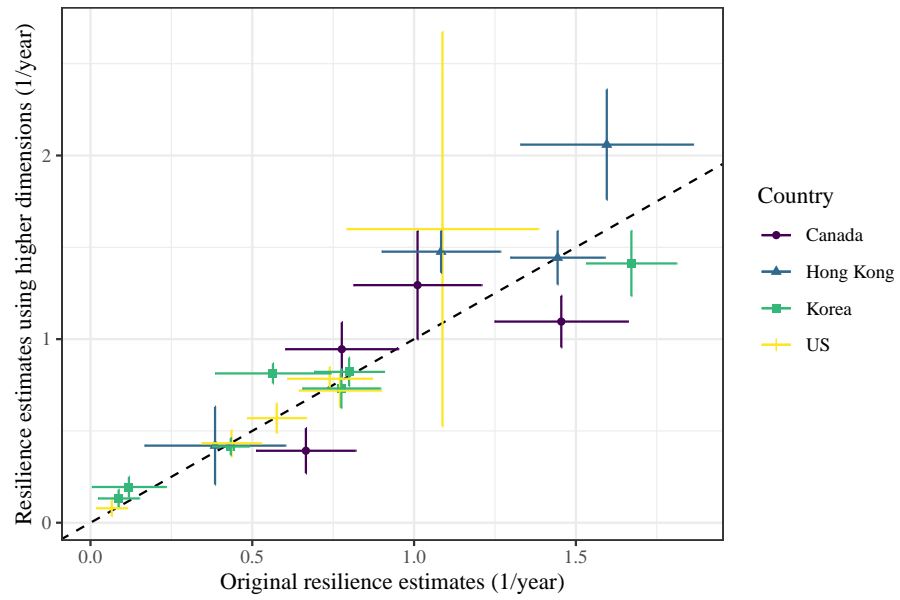


Figure S12: **Comparison of resilience estimates.** Each point represents a resilience estimate for a specific pathogen at a specific country. The x values represent the original resilience estimates presented in Figure 4. The y values represent the original resilience estimates presented in Supplementary Figure S11.

642 References

- 643 [1] Rachel E Baker, Sang Woo Park, Wenchang Yang, Gabriel A Vecchi, C Jessica E
644 Metcalf, and Bryan T Grenfell. The impact of COVID-19 nonpharmaceutical
645 interventions on the future dynamics of endemic infections. *Proceedings of the*
646 *National Academy of Sciences*, 117(48):30547–30553, 2020.
- 647 [2] Gabriela B Gomez, Cedric Mahé, and Sandra S Chaves. Uncertain effects of the
648 pandemic on respiratory viruses. *Science*, 372(6546):1043–1044, 2021.
- 649 [3] Mihaly Koltai, Fabienne Krauer, David Hodgson, Edwin van Leeuwen, Marina
650 Treskova-Schwarzbach, Mark Jit, and Stefan Flasche. Determinants of RSV
651 epidemiology following suppression through pandemic contact restrictions. *Epi-*
652 *demics*, 40:100614, 2022.
- 653 [4] Sang Woo Park, Brooklyn Noble, Emily Howerton, Bjarke F Nielsen, Sarah
654 Lentz, Lilliam Ambroggio, Samuel Dominguez, Kevin Messacar, and Bryan T
655 Grenfell. Predicting the impact of non-pharmaceutical interventions against
656 COVID-19 on *Mycoplasma pneumoniae* in the United States. *Epidemics*,
657 49:100808, 2024.
- 658 [5] Amanda C Perofsky, Chelsea L Hansen, Roy Burstein, Shanda Boyle, Robin
659 Prentice, Cooper Marshall, David Reinhart, Ben Capodanno, Melissa Truong,
660 Kristen Schwabe-Fry, et al. Impacts of human mobility on the citywide trans-
661 mission dynamics of 18 respiratory viruses in pre-and post-COVID-19 pandemic
662 years. *Nature communications*, 15(1):4164, 2024.
- 663 [6] Eric J Chow, Timothy M Uyeki, and Helen Y Chu. The effects of the COVID-19
664 pandemic on community respiratory virus activity. *Nature Reviews Microbiol-*
665 *ogy*, 21(3):195–210, 2023.
- 666 [7] Stephen M Kissler, Christine Tedijanto, Edward Goldstein, Yonatan H Grad,
667 and Marc Lipsitch. Projecting the transmission dynamics of SARS-CoV-2
668 through the postpandemic period. *Science*, 368(6493):860–868, 2020.
- 669 [8] Rachel E Baker, Chadi M Saad-Roy, Sang Woo Park, Jeremy Farrar, C Jessica E
670 Metcalf, and Bryan T Grenfell. Long-term benefits of nonpharmaceutical inter-
671 ventions for endemic infections are shaped by respiratory pathogen dynamics.
672 *Proceedings of the National Academy of Sciences*, 119(49):e2208895119, 2022.
- 673 [9] John-Sebastian Eden, Chisha Sikazwe, Ruopeng Xie, Yi-Mo Deng, Sheena G
674 Sullivan, Alice Michie, Avram Levy, Elena Cutmore, Christopher C Blyth,
675 Philip N Britton, et al. Off-season RSV epidemics in Australia after easing
676 of COVID-19 restrictions. *Nature communications*, 13(1):2884, 2022.
- 677 [10] Stuart L Pimm. The structure of food webs. *Theoretical population biology*,
678 16(2):144–158, 1979.

- 679 [11] Michael G Neubert and Hal Caswell. Alternatives to resilience for measuring
680 the responses of ecological systems to perturbations. *Ecology*, 78(3):653–665,
681 1997.
- 682 [12] Lance H Gunderson. Ecological resilience—in theory and application. *Annual
683 review of ecology and systematics*, 31(1):425–439, 2000.
- 684 [13] Vasilis Dakos and Sonia Kéfi. Ecological resilience: what to measure and how.
685 *Environmental Research Letters*, 17(4):043003, 2022.
- 686 [14] Georgiy V Bobashev, Stephen P Ellner, Douglas W Nychka, and Bryan T
687 Grenfell. Reconstructing susceptible and recruitment dynamics from measles
688 epidemic data. *Mathematical Population Studies*, 8(1):1–29, 2000.
- 689 [15] Bärbel F Finkenstädt and Bryan T Grenfell. Time series modelling of childhood
690 diseases: a dynamical systems approach. *Journal of the Royal Statistical Society
691 Series C: Applied Statistics*, 49(2):187–205, 2000.
- 692 [16] Floris Takens. Detecting strange attractors in turbulence. In *Dynamical Sys-
693 tems and Turbulence, Warwick 1980: proceedings of a symposium held at the
694 University of Warwick 1979/80*, pages 366–381. Springer, 2006.
- 695 [17] Alan Hastings, Karen C Abbott, Kim Cuddington, Tessa Francis, Gabriel Gell-
696 ner, Ying-Cheng Lai, Andrew Morozov, Sergei Petrovskii, Katherine Scran-
697 ton, and Mary Lou Zeeman. Transient phenomena in ecology. *Science*,
698 361(6406):eaat6412, 2018.
- 699 [18] Matthew B Kennel, Reggie Brown, and Henry DI Abarbanel. Determining
700 embedding dimension for phase-space reconstruction using a geometrical con-
701 struction. *Physical review A*, 45(6):3403, 1992.
- 702 [19] Eugene Tan, Shannon Algar, Débora Corrêa, Michael Small, Thomas Stemler,
703 and David Walker. Selecting embedding delays: An overview of embedding
704 techniques and a new method using persistent homology. *Chaos: An Interdis-
705 ciplinary Journal of Nonlinear Science*, 33(3), 2023.
- 706 [20] Samit Bhattacharyya, Per H Gesteland, Kent Korgenski, Ottar N Bjørnstad,
707 and Frederick R Adler. Cross-immunity between strains explains the dynamical
708 pattern of paramyxoviruses. *Proceedings of the National Academy of Sciences*,
709 112(43):13396–13400, 2015.
- 710 [21] Bryan T Grenfell, Ottar N Bjørnstad, and Bärbel F Finkenstädt. Dynamics of
711 measles epidemics: scaling noise, determinism, and predictability with the TSIR
712 model. *Ecological monographs*, 72(2):185–202, 2002.

- 713 [22] Virginia E Pitzer, Cécile Viboud, Vladimir J Alonso, Tanya Wilcox, C Jessica
714 Metcalf, Claudia A Steiner, Amber K Haynes, and Bryan T Grenfell. Environmental drivers of the spatiotemporal dynamics of respiratory syncytial virus in
715 the United States. *PLoS pathogens*, 11(1):e1004591, 2015.
- 716
- 717 [23] Katharine R Dean, Fabienne Krauer, Lars Walløe, Ole Christian Lingjærde, Barbara Bramanti, Nils Chr Stenseth, and Boris V Schmid. Human ectoparasites
718 and the spread of plague in Europe during the Second Pandemic. *Proceedings
719 of the National Academy of Sciences*, 115(6):1304–1309, 2018.
- 720
- 721 [24] Margarita Pons-Salort and Nicholas C Grassly. Serotype-specific immunity
722 explains the incidence of diseases caused by human enteroviruses. *Science*,
723 361(6404):800–803, 2018.
- 724
- 725 [25] Sarah Cobey and Edward B Baskerville. Limits to causal inference with state-
space reconstruction for infectious disease. *PloS one*, 11(12):e0169050, 2016.
- 726
- 727 [26] Edward Goldstein, Sarah Cobey, Saki Takahashi, Joel C Miller, and Marc Lipsitch.
Predicting the epidemic sizes of influenza A/H1N1, A/H3N2, and B: a
728 statistical method. *PLoS medicine*, 8(7):e1001051, 2011.
- 729
- 730 [27] Bob Carpenter, Andrew Gelman, Matthew D Hoffman, Daniel Lee, Ben
Goodrich, Michael Betancourt, Marcus A Brubaker, Jiqiang Guo, Peter Li,
731 and Allen Riddell. Stan: A probabilistic programming language. *Journal of
statistical software*, 76, 2017.
- 732
- 733 [28] Stan Development Team. RStan: the R interface to Stan, 2024. R package
734 version 2.32.6.